

Eyewall Asymmetries and Their Contributions to the Intensification of an Idealized Tropical Cyclone Translating in Uniform Flow

JONATHAN MARTINEZ,^a CHRISTOPHER A. DAVIS,^a AND MICHAEL M. BELL^b

^a National Center for Atmospheric Research, Boulder, Colorado

^b Colorado State University, Fort Collins, Colorado

(Manuscript received 15 November 2021, in final form 27 May 2022)

ABSTRACT: Scale-dependent processes within the tropical cyclone (TC) eyewall and their contributions to intensification are examined in an idealized simulation of a TC translating in uniform environmental flow. The TC circulation is partitioned into axisymmetric, low-wavenumber ($m = 1\text{--}3$), and high-wavenumber ($m > 3$) categories, and scale-dependent contributions to the intensification process are quantified through the azimuthal-mean relative (vertical) vorticity and tangential momentum budgets. To further account for the interdependent relationship between the axisymmetric vortex structure and eyewall asymmetries, the analyses are subdivided into three periods—early, middle, and late—that represent the approximate quartiles of the full intensification period prior to the TC attaining its maximum intensity. The asymmetries become concentrated among lower azimuthal wavenumbers during the intensification process and are persistently distributed among a broader range of azimuthal scales at higher altitudes. The scale-dependent budgets demonstrate that the axisymmetric and asymmetric processes generally oppose each other during TC intensification. The axisymmetric processes are mostly characterized by a radial spinup dipole pattern, with a tangential momentum spinup tendency concentrated along the radius of maximum tangential winds (RMW) and a spindown tendency concentrated radially inward of the RMW. The asymmetric processes are mostly characterized by an opposing spindown dipole pattern that is slightly weaker in magnitude. The most salient exception occurs from high-wavenumber processes contributing to a relatively modest, net spinup along the RMW between ~ 2 - and 4-km altitude. Given that the maximum tangential winds persistently reside below 2-km altitude, eyewall asymmetries are primarily found to impede TC intensification.

SIGNIFICANCE STATEMENT: The convection fueling a tropical cyclone progressively organizes into a compact region called the eyewall where the strongest winds and rainfall occur. As the tropical cyclone intensifies, convection in the circular eyewall becomes more uniform, and the eyewall takes the appearance of a ring. We call this ring shape the “symmetric” part of the eyewall. As convection in the eyewall evolves and interacts, the eyewall becomes deformed and develops wiggles. We call these wiggly shapes the “asymmetric” parts of the eyewall. We demonstrate that the symmetric part of the eyewall helps intensification. The asymmetric parts of the eyewall mostly hurt intensification except during the earlier stages. Our results indicate that a symmetric eyewall shape is preferable for tropical cyclone intensification.

KEYWORDS: Tropical cyclones; Hurricanes/typhoons; Mesoscale processes; Momentum; Vorticity; Mesoscale models; Numerical analysis/modeling

1. Introduction

Early radar observations of convection within the tropical cyclone (TC) eyewall depicted substantial deviations from axial symmetry in the reflectivity field, and in many cases the TC eyewall was observed to cycle between various polygonal shapes with vertices connected by straight-line segments (Lewis and Hawkins 1982; Muramatsu 1986). An expanding record of observations indicates that the TC eyewall generally comprises a continuum of asymmetries, ranging from turbulent roll clouds, convective bursts, and misoscale vortices, to polygonal eyewall shapes, mesovortices, and mesoscale convective systems. Despite growing observational evidence supporting the near ubiquity of TC eyewall asymmetries, asymmetric contributions to the intensification process remain unclear. Do eyewall asymmetries facilitate or impede TC

intensification? Or could the dichotomy be an oversimplification, and might there be a variety of circumstances where asymmetries could facilitate or impede TC intensification?

Through a combination of sustained updraft mass flux via the overturning, transverse circulation and periodic bursts of anomalous updraft mass fluxes varying in scale, convection within the TC eyewall progressively concentrates potential vorticity (PV) along its radially inward flank, extending throughout much of the troposphere. The emergent vortex structure in the eyewall region thus resembles an annulus of relatively high-PV air in the horizontal plane, a “tower” of high-PV air in the azimuthal-mean, radius–altitude plane (Schubert et al. 1999), and a “bowl” of high-PV air in three dimensions (Hausman et al. 2006). The radial PV gradients accompanying such an annulus of high-PV air produce waveguides for vortex Rossby waves (VRWs; Guinn and Schubert 1993; Montgomery and Kallenbach 1997), akin to the meridional gradient of planetary vorticity producing a waveguide for planetary Rossby waves. Schubert et al. (1999)

Corresponding author: Jonathan Martinez, jmart@ucar.edu

demonstrated that exponential instability can arise from the mutual amplification of counterpropagating VRWs orbiting the TC eyewall, such that PV concentrated near the eyewall region pools into mesovortices that constitute the vertices of polygonal eyewall structures. Through continued mixing between the low-PV air in the eye region and high-PV air in the eyewall, the inner-core vortex structure transitions to a PV monopole; that is, PV is maximized near the axis of rotation and monotonically decreases with radius. Several observational studies have documented the evolution of eyewall mesovortices during various stages of the TC life cycle (e.g., Kuo et al. 1999; Kossin et al. 2002; Bell and Montgomery 2008; Wurman and Kosiba 2018). In a few cases, polygonal eyewall structures and mesovortices have been observed during periods of TC intensification (Hendricks et al. 2012; Wurman and Kosiba 2018; Cha et al. 2021), further stimulating questions about the potential contributions from asymmetric processes to TC intensification.

Nondivergent, barotropic modeling studies have demonstrated that PV mixing associated with barotropic instability decreases the central pressure, but it also decreases the maximum azimuthal-mean tangential winds (Schubert et al. 1999; Kossin and Schubert 2001; Hendricks et al. 2009). Although nondivergent, barotropic simulations of PV mixing produce an overall reduction in the vortex intensity, forced barotropic simulations reveal a “dual nature” to PV mixing. For example, Rozoff et al. (2009) added an axisymmetric, logically limited vorticity source to the nondivergent, barotropic model as an idealized representation of the sustained diabatic forcing found in a TC eyewall. Rozoff et al. found that individual PV mixing events induced by barotropic instability produce transient intensification breaks as high-PV air is mixed from the eyewall into the eye, but that successive PV mixing events can produce a cumulative transport of high-PV air from the eyewall into the eye such that the vortex attains a higher intensity than it would have otherwise. Hendricks et al. (2014) generalized the framework from Rozoff et al. (2009) to a forced, shallow water model and found that barotropic instability results in the high-PV annulus rolling up into convective (diabatic) mesovortices. In a simulation where the forcing was prescribed as proportional to the relative vorticity, Hendricks et al. demonstrated that convective mesovortices contributed to simultaneously reducing the minimum pressure and increasing the maximum tangential winds during the barotropic instability process. The foregoing discussion illustrates a variety of end states arising from barotropic instability in the TC eyewall, with nondivergent, barotropic models mostly indicating vortex weakening and with models of increasing complexity indicating the potential for vortex intensification.

An alternative framework to investigate how asymmetric processes contribute to TC intensification entails forcing an axisymmetric vortex with asymmetric perturbations, such that the vortex end state represents a cumulative adjustment solely brought about by asymmetries. Möller and Montgomery (2000) demonstrated that repetitive injections of asymmetric PV into the TC eyewall could contribute to intensification through a transfer of energy from the asymmetries to the basic-state vortex (i.e., axisymmetrization). Asymmetric PV

perturbations were considered the end product of a rapid adjustment process resulting from convective heating sources, and thus Möller and Montgomery proposed that convective “pulsing” could be an important asymmetric process contributing to TC intensification. Nolan and Grasso (2003) further investigated the response of an axisymmetric basic-state vortex in thermal wind balance to asymmetric perturbations by using a three-dimensional, nonhydrostatic model developed from the linearized, anelastic equations of motion (Nolan and Montgomery 2002). Rather than superposing asymmetric PV perturbations onto an axisymmetric basic-state vortex, instantaneous asymmetric thermal perturbations were introduced to represent the rapid latent heat release in convective updrafts. Therefore, a more realistic evolution was captured by incorporating the full adjustment process of the basic-state axisymmetric vortex circulation to instantaneous, asymmetric thermal forcing. Asymmetric PV perturbations generated from the asymmetric thermal forcing first underwent a transient growth period prior to axisymmetrization. Nolan and Grasso inferred that the transient growth period of the asymmetric PV perturbations contributed to a net weakening of the vortex circulation when intensity is defined as the azimuthal-mean surface tangential winds along the radius of maximum tangential winds (RMW). Nolan et al. (2007) further generalized the linear, three-dimensional model from Nolan and Grasso (2003) to incorporate time varying heat sources that evolve with the axisymmetric vortex circulation and also found that asymmetric thermal forcing contributed to a net weakening of the vortex circulation. Although the comprehensive set of experiments investigated by Nolan and Grasso and Nolan et al. primarily indicate that asymmetries contribute to a weakening of the axisymmetric vortex circulation, it remains unclear to what extent the aggregate findings from their linearized simulations can be generalized to TCs that experience fully nonlinear processes in the presence of moist convection.

Simulations of TC intensification that incorporate fully nonlinear, moist convective processes exhibit many of the asymmetric structures that emerge in more simplified modeling frameworks, but further capture a coupling between eyewall asymmetries and convection that may have implications for the intensification process. Yang et al. (2007) found that the resolved asymmetries of a TC simulated in a quiescent environment reduced the wind speed near the RMW by transporting high momentum air from the TC eyewall into the eye, and thus asymmetries were noted to reduce TC intensity. Nolan et al. (2017) simulated a tornado-like vortex within a large-eddy simulation framework. Although the vortex intensification dynamics vary between TCs and tornadoes, Nolan et al. found that the resolved asymmetries developing in the vortex core tend to spin down the maximum azimuthal-mean tangential winds by transporting angular momentum inward and upward relative to the RMW, similar to the findings from Yang et al. (2007). Nguyen et al. (2011) and Hankinson et al. (2014) found that the simulated intensification of Hurricane Katrina (2005) was characterized by “vacillation cycles.” PV mixing events were intermediated by periods of relatively slower intensification during the transition toward a monopole

structure and periods of relatively quicker intensification as the PV annulus was restored near the eyewall. [Hardy et al. \(2021\)](#) analyzed an ensemble simulation that captured the rapid intensification of Typhoon Neptak (2016) and noted similar vacillation cycles among 60% of their ensemble members. Recent studies have emphasized the importance of asymmetric convective processes within the TC eyewall in ventilating mass converging within the boundary layer, thereby inhibiting the frictional spindown tendency induced by the boundary layer and contributing to a spinup of tangential winds above the boundary layer (e.g., see the discussion in section 3.5 of [Montgomery and Smith 2017; Hardy et al. 2021; Montgomery et al. 2021; Smith et al. 2021](#)). [Persing et al. \(2013\)](#) found that asymmetric processes can also exhibit up-gradient characteristics during TC intensification, contributing both to a contraction of the RMW and a spinup of the maximum axisymmetric tangential winds. [Bhalachandran et al. \(2020\)](#) found that the primary asymmetric growth and decay processes in their simulation of TC Phalin (2013) occurred largely independent from the axisymmetric vortex circulation, leading the authors to cast doubt that “eddies only grow at the expense of the mean.” Collectively, simulations that incorporate fully nonlinear, moist convective processes illustrate viable pathways for asymmetric processes to either facilitate or impede TC intensification, and such pathways may stem from a coupling between eyewall asymmetries and convection that is absent in more idealized simulations.

The primary objective of the present study is to examine a continuum of asymmetries evolving near the eyewall of an idealized TC translating in uniform flow, and to quantify asymmetric contributions to the intensification process. The evolution of asymmetries within the TC circulation is interdependent with the evolution of the axisymmetric vortex; that is, the contributions from asymmetric processes to the axisymmetric vortex depend on the axisymmetric vortex structure itself, and vice versa. Therefore, the analyses presented herein will be divided into three periods during the intensification process to account for the structural evolution of the axisymmetric vortex. The following section will describe the initial conditions for the idealized TC simulation, [section 3](#) will discuss the numerical model simulation design and analysis methods, [section 4](#) will present results from three periods during the intensification process, [section 5](#) will comprehensively discuss the results from each time period during the intensification process, and [section 6](#) will provide concluding remarks and potential avenues for future work.

2. Initial environment and vortex structure

The idealized TC simulation is initialized with a horizontally homogeneous environment that is characteristic of the climatological-mean atmospheric conditions observed in the Caribbean and North Atlantic basin during the July–October hurricane season ([Dunion 2011](#)). A weak, cyclonic vortex representing a tropical depression is superposed on the initial environment to facilitate the development of a TC. Precursor disturbances to cyclogenesis are often characterized by a

broad cyclonic circulation comprising a midlevel vortex (e.g., [McBride and Zehr 1981; Bister and Emanuel 1997; Gray 1998; Raymond et al. 2011](#)). The cyclonic PV anomaly that accompanies a midlevel vortex is balanced by a relatively warm potential temperature anomaly above its circulation and a relatively cool potential temperature anomaly below ([Raymond and Jiang 1990; Raymond et al. 2014](#)). Collectively, information gathered from the aforementioned studies suggests that an initial vortex representing a tropical depression should possess a broad cyclonic circulation with maximum winds displaced above the surface. Therefore, the initial radial vortex structure is constructed from a modified Rankine vortex of the form

$$v_0(r) = \begin{cases} v_{\max} \left(\frac{r}{r_{\max}} \right), & 0 \leq r < r_{\max}, \\ v_{\max} \left(\frac{r}{r_{\max}} \right)^{-\alpha}, & r \geq r_{\max}, \end{cases} \quad (1)$$

where $v_{\max} = 15 \text{ m s}^{-1}$ is the maximum tangential velocity, r the radius, $r_{\max} = 135 \text{ km}$ is the RMW, and $\alpha = 0.3$ is the decay of tangential velocity radially outward of the RMW. [Ritchie and Holland \(1999\)](#) constructed a similar initial vortex for their idealized simulations based on the composite observations of tropical depressions from [McBride and Zehr \(1981\)](#). Following [Nolan \(2007\)](#), a radial decay function is applied to the initial vortex structure radially outward of the RMW, ensuring that the total circulation within the doubly periodic model domain is zero. The radial decay function is given by

$$v(r) = v_0(r) \exp \left[\left(-\frac{r}{R} \right)^6 \right], \quad (2)$$

where $v_0(r)$ is the initial modified Rankine vortex given by (1) and $R = 600 \text{ km}$.

The initial vortex is then extended in the vertical following [Nolan \(2007\)](#), such that the initial axisymmetric vortex structure is given by

$$v(r, z) = v(r) \exp \left(-\frac{|z - z_{\max}|^\beta}{\beta L_z^\beta} \right), \quad (3)$$

where $v(r)$ is the initial modified Rankine vortex after the radial decay function has been applied, z the altitude, z_{\max} the altitude of maximum tangential velocity, L_z the depth of an approximately barotropic region of the vortex, and β the vertical decay of tangential velocity above and below the barotropic region. To construct a tropical depression with maximum tangential velocity displaced above the surface, z_{\max} is set to 1.5 km , L_z is set to 2.5 km above z_{\max} and 3.5 km below z_{\max} , and β is set to 1.8 . The initial axisymmetric vortex is characterized by a maximum surface tangential velocity of $\sim 12 \text{ m s}^{-1}$ with an $\sim 3\text{-K}$ warm potential temperature anomaly above 1.5-km altitude and an $\sim 3\text{-K}$ cool potential temperature anomaly below 1.5-km altitude, with both anomalies relative to the environment.

3. Simulation design and analysis methods

a. Numerical model setup

The idealized TC is simulated with the nonhydrostatic, fully compressible Cloud Model 1 (CM1) version 19.7 (Bryan and Fritsch 2002). The horizontal grid is structured within a doubly periodic domain comprising 1140×1140 grid points that span $2670 \text{ km} \times 2670 \text{ km}$. The horizontal grid spacing is a uniform 1 km for the innermost $800 \text{ km} \times 800 \text{ km}$ and smoothly transitions to 10-km spacing at the domain boundaries. The vertical grid comprises 76 levels that span 26 km in altitude. The vertical grid spacing is a uniform 100 m in the lowest 2-km altitude and smoothly transitions to 500-m spacing at 8-km altitude; above 8-km altitude, the vertical grid spacing is a uniform 500 m. A Rayleigh damping layer is placed above 22-km altitude to mitigate the reflection of internal gravity waves.

The TC simulation is integrated for seven days on an f plane corresponding to $\sim 15^\circ\text{N}$. Sea surface temperatures are fixed at 28°C and uniform throughout the simulation domain. To approximate clear-sky radiative processes, a simple Newtonian cooling of 2 K day^{-1} is applied throughout the simulation that relaxes the domain-averaged temperature profile toward its base state (Rotunno and Emanuel 1987). The Morrison double-moment microphysics scheme is chosen to parameterize microphysical processes with graupel selected for the large ice category (Bryan and Morrison 2012). Subgrid-scale turbulence is parameterized with a first-order, local closure scheme wherein the horizontal eddy viscosity is determined from the horizontal flow deformation, and the vertical eddy viscosity is determined from the vertical flow deformation and the moist Brunt–Väisälä frequency (e.g., Bryan et al. 2017). The horizontal and vertical mixing lengths required for this subgrid-scale turbulence parameterization are set as $l_h = 1000 \text{ m}$ and $l_v = 100 \text{ m}$, respectively.

To approximate the first-order evolution of TCs observed in nature and facilitate the development of eyewall asymmetries, a 5 m s^{-1} uniform easterly flow is gradually imposed throughout the model domain. The details of the large-scale wind acceleration and nudging methodology implemented in CM1 can be found in the appendix of Alland et al. (2021). Briefly, the uniform easterly flow is implemented in CM1 through the addition of acceleration terms to the governing equations for horizontal momentum that approximate a large-scale pressure gradient. The domain-averaged zonal winds are nudged toward the prescribed, uniform easterly reference wind profile, and thus a net circulation is not introduced into the model domain. The meridional temperature gradient required to satisfy thermal wind balance is neglected for simplicity given the doubly periodic model boundary conditions. The uniform easterly flow is introduced 12 h into the simulation with a 6-h nudging time scale, permitting the incipient vortex to develop deep, moist convection prior to initiating its translation. A time-varying translational domain is created by tracking the minimum of a smoothed surface-pressure field that represents the approximate vortex center of circulation. The vortex center of circulation is further

refined to minimize errors from aliasing the axisymmetric vortex circulation onto higher-order asymmetries (Ryglicki and Hodyss 2016). For a given model level, the center of circulation is determined from a simplex algorithm that iteratively maximizes the tangential circulation within a 5-km annulus centered on a first-guess RMW [see section 2 of Bell and Lee (2012) and precise details in section 3.3 of Martinez (2020)]. The center of circulation is layer averaged between the surface and 3-km altitude and used to calculate time-varying, storm-relative winds.

b. Spectral binning and Reynolds averaging

An arbitrary scalar or vector ψ can be partitioned into components representing axial symmetry and deviations from axial symmetry (asymmetries) by representing its azimuthal dimension ϕ as a Fourier series given by

$$\psi_m(r, z, t) = \sum_{j=0}^{J-1} \psi(r, j, z, t) e^{-i2\pi mj/J}, \quad \text{for } m = 0, 1, 2, \dots, 180, \quad (4)$$

where $\psi(r, j, z, t)$ is the arbitrary quantity of interest in cylindrical coordinates, m the azimuthal wavenumber, r the radius, j an integer representing the azimuthal angle increment ($j = 0, 1, 2, \dots, J = 360$), z the altitude, and t the time. Thus, the axisymmetric component is given by the Fourier coefficient ψ_0 and the full spectrum of asymmetries is given by the Fourier coefficients ψ_m for $m = 1, 2, 3, \dots, 180$.

Asymmetries are partitioned into low and high azimuthal wavenumbers for all scalar and vector quantities, representing relatively large and small azimuthal scales, respectively. As will be shown later, the distribution of spectral power among azimuthal wavenumbers in the vortex circulation exhibits variance as a function of altitude and time. Therefore, spectral binning into categories of low and high wavenumbers is somewhat arbitrary, and no precise definition exists in the literature. Herein, low-wavenumber asymmetric structures are defined by azimuthal wavenumbers $m = 1\text{--}3$ and high-wavenumber asymmetric structures by azimuthal wavenumbers $m = 4\text{--}180$.¹ Despite the aforementioned limitations, the low- and high-wavenumber categorization provides a useful conceptual framework to distinguish scale-dependent contributions from asymmetries to TC intensification. The low-wavenumber category falls in between the $m = 1\text{--}2$ definition from Bhalachandran et al. (2020) and the $m = 1\text{--}4$ definition from Reasor et al. (2009). In applying the spectral binning, ψ is now given by

$$\psi(r, \phi, z, t) = \bar{\psi}(r, z, t) + \psi_l'(r, \phi, z, t) + \psi_h'(r, \phi, z, t), \quad (5)$$

where the overbar denotes the axisymmetric component, primes denote the asymmetric components, and the subscripts l and h further denote the low- and high-wavenumber

¹ The azimuthal dimension is defined for the interval $[0, 2\pi]$ in increments of $\pi/180$, giving $J = 360$ azimuthal grid points. Therefore, $m = 180$ is the Nyquist wavenumber.

categories, respectively. In accordance with Reynolds averaging, the average product of two partitioned quantities ψ_1 and ψ_2 is given by

$$\begin{aligned}\overline{\psi_1 \psi_2} &= \overline{(\psi_{1,l} + \psi'_{1,l} + \psi_{1,h})(\psi_{2,l} + \psi'_{2,l} + \psi_{2,h})} \\ &= \overline{\psi_1} \overline{\psi_2} + \overline{\psi'_{1,l} \psi'_{2,l}} + \overline{\psi'_{1,h} \psi'_{2,h}}.\end{aligned}\quad (6)$$

c. The vorticity equation

The evolution of relative (vertical) vorticity is given in flux form by

$$\frac{\partial \zeta}{\partial t} = -\nabla \cdot (\zeta \mathbf{U} - w \boldsymbol{\xi} + \hat{\mathbf{k}} \times \mathbf{F}), \quad (7)$$

where \mathbf{U} is the three-dimensional velocity vector comprising the radial u , azimuthal v , and vertical w velocity components; $\boldsymbol{\xi}$ the three-dimensional relative vorticity vector comprising the radial ξ , azimuthal, and vertical ζ vorticity components; $\hat{\mathbf{k}}$ the unit vector oriented along the vertical axis; \mathbf{F} the three-dimensional diffusive tendency of momentum comprising the subgrid-scale turbulence parameterization described in section 3a; and ∇ the two-dimensional divergence operator in the horizontal plane.

To formulate the flux form of the azimuthal-mean relative vorticity equation, the azimuthal wavenumber partitioning and Reynolds averaging from the previous section are applied to (7), such that

$$\begin{aligned}\frac{\partial \bar{\zeta}}{\partial t} &= -\frac{\partial(r\bar{u}\bar{\zeta})}{r\partial r} - \frac{\partial(r\bar{u}'_l\bar{\zeta}'_l)}{r\partial r} - \frac{\partial(r\bar{u}'_h\bar{\zeta}'_h)}{r\partial r} + \frac{\partial(r\bar{w}\bar{\xi})}{r\partial r} + \frac{\partial(r\bar{w}'_l\bar{\xi}'_l)}{r\partial r} \\ &\quad + \frac{\partial(r\bar{w}'_h\bar{\xi}'_h)}{r\partial r} + \frac{\partial(r\bar{F}_\phi)}{r\partial r}.\end{aligned}\quad (8)$$

The first three terms in Eq. (8) represent contributions to the azimuthal-mean relative vorticity $\bar{\zeta}$ tendency arising from the radial divergence of 1) radial fluxes of axisymmetric relative vorticity, 2) radial fluxes of low-wavenumber relative vorticity, and 3) radial fluxes high-wavenumber relative vorticity; the following three terms represent contributions to the $\bar{\zeta}$ tendency arising from the radial divergence of 4) tilting axisymmetric radial vorticity, 5) tilting low-wavenumber radial vorticity, and 6) tilting high-wavenumber radial vorticity; and the last term represents contributions to the $\bar{\zeta}$ tendency arising from the radial divergence of diffusive processes that oppose the tangential circulation.

4. Structural evolution during the intensification period

a. Vortex intensification and symmetry

The initiation of rapid intensification (RI) is defined for the simulated TC following the approximate 95th percentile of 24-h overwater TC intensification rates in the North Atlantic basin, corresponding to a 24-h intensification of 15.4 m s^{-1} (Kaplan et al. 2010), and is further refined by requiring each consecutive 6-h intensification within the 24-h time window to exceed 3.8 m s^{-1} . Given the two criteria listed above, the

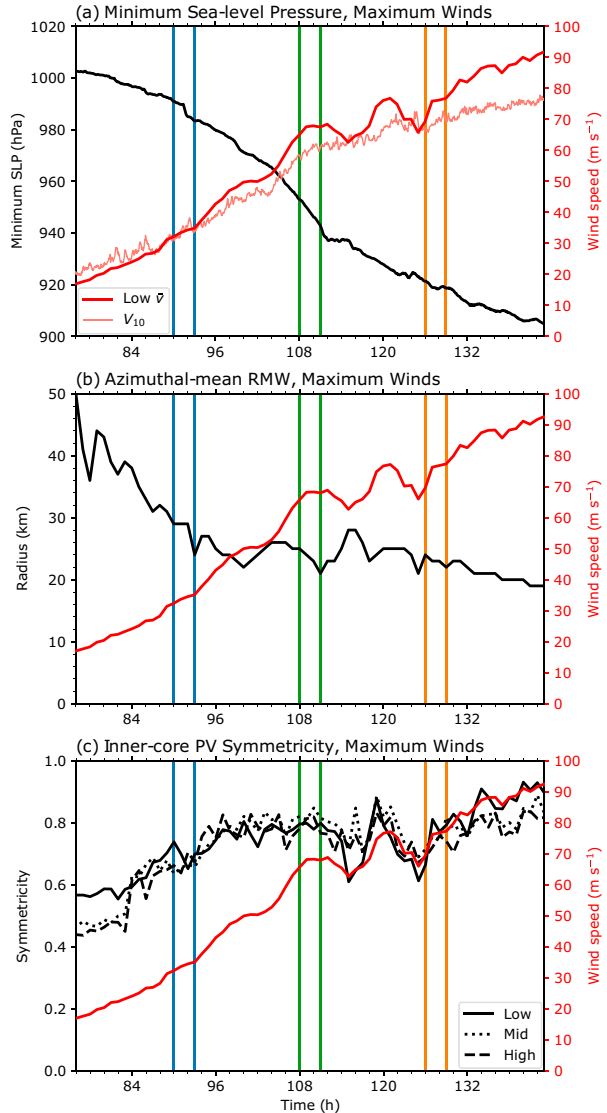


FIG. 1. Time series of the vortex evolution are shown during the intensification period ($t = 76$ – 143 h). (a) The maximum wind speed 10 m above the ocean surface (light red) and the minimum sea level pressure (black) are shown with 1-min model output. (b) The azimuthal-mean radius of maximum tangential winds (RMW) is shown at the lowest model level ($z = 50 \text{ m}$) with 1-h model output. (c) The inner-core potential vorticity (PV) symmetry is shown for each of the following vertical layers in the vortex circulation: the low layer ($z = 0$ – 3 km), midlayer ($z = 3$ – 6 km), and high layer ($z = 6$ – 9 km). The dark red line in each panel denotes the low-layer-averaged, azimuthal-mean tangential winds with 1-h model output. The vertical, colored lines represent the three time windows analyzed during the intensification period: early rapid intensification (RI; blue; $t = 90$ – 93 h), mid-RI (green; $t = 108$ – 111 h), and late RI (orange; $t = 126$ – 129 h).

initiation of RI is calculated from a smoothed time series of the maximum wind speed 10 m above the ocean surface (see the thin, light-red line in Fig. 1a). The time period of interest for this study occurs between the initiation of RI and maximum

intensity, henceforth defined as the intensification period. During the 67-h intensification period, the TC intensifies 70 m s^{-1} , deepens 100 hPa, and the RMW contracts approximately 30 km (Fig. 1).

To assess the bulk evolution of asymmetric structures during the intensification period, the magnitude of inner-core asymmetries is first compared to the magnitude of the axisymmetric vortex. The magnitude of symmetry, often referred to as the “symmetricity,” can be quantified for an arbitrary scalar or vector ψ as

$$S_\psi = \frac{\overline{|\psi|}}{|\overline{\psi}| + \frac{1}{2\pi} \int_0^{2\pi} |\psi| \partial\phi}. \quad (9)$$

Thus, S_ψ represents the absolute deviation from axial symmetry, similar to the squared deviation described in previous studies (Miyamoto and Takemi 2013; Miyamoto and Nolan 2018). S_ψ is defined between 0 and 1 with 0 denoting an entirely asymmetric structure and 1 denoting an entirely axisymmetric structure. The variability of asymmetric structures as a function of altitude is assessed by considering the following three layers in the vortex circulation: 0–3-km altitude (low layer), 3–6-km altitude (middle layer), and 6–9-km altitude (high layer). The inner-core region of the vortex circulation is approximated by the area between the axis of rotation and $1.5 \times \text{RMW}$, where the RMW is averaged over each respective layer. Symmetricity is computed for the mass-weighted, layer-averaged PV between each respective layer and then area averaged over the inner-core region.

Figure 1c shows time series of the inner-core symmetricity during the intensification period for each layer in the vortex circulation. Throughout the intensification period, the azimuthal distribution of inner-core PV for each layer generally fluctuates between ~60% and 80% symmetricity and the vortex gradually becomes increasingly axisymmetric; however, axisymmetry is never attained during the intensification period. Instead, the inner-core circulation remains nearly 10% asymmetric at its peak symmetricity, occurring near the end of the intensification period. There is a relative slowdown in the overall evolution of the vortex circulation that occurs near the approximate midway point of the intensification period ($t = 108 \text{ h}$), denoted by a diminishing rate of intensification, contraction, and symmetrization (Figs. 1a–c).

To further investigate the asymmetric vortex structure during the intensification period, the azimuthal scales of inner-core PV asymmetries are analyzed by constructing a mass-weighted PV power spectrum for each layer in the vortex circulation. As in the symmetricity analysis, the mass-weighted PV power spectra are area averaged over the inner-core region. Figure 2 shows the normalized power spectra and corresponding cumulative normalized power spectra for each layer as a function of azimuthal wavenumber m and time during the intensification period.

Although the PV symmetricity for each layer in the vortex circulation is nearly equivalent throughout the intensification period (Fig. 1c), Fig. 2 demonstrates that the inner-core asymmetric PV is distributed among a broader range of azimuthal

scales at higher altitudes. Furthermore, the temporal variability in the azimuthal distribution of asymmetric PV increases as a function of altitude in the vortex circulation, denoted by relatively larger oscillations in the 90% cumulative normalized power contour (cyan in Figs. 2d–f). In general, the vortex progresses toward a more compact, axisymmetric circulation while the inner-core asymmetric PV distribution progresses toward lower azimuthal wavenumbers (i.e., larger azimuthal scales) throughout the intensification period. However, the slowdown in the evolution of the vortex circulation noted above is also evident in the asymmetric PV evolution; the approximate midway point of the intensification period is characterized by a diminishing rate of asymmetric PV concentration among lower azimuthal wavenumbers. Results up to this point have demonstrated that the inner-core distribution of PV is never fully axisymmetric during the intensification period and that PV asymmetries are dynamic, possessing structural and temporal variability throughout the vortex circulation.

b. General vortex structure

Axisymmetric and asymmetric components of the vortex structure are examined for three time slices during the intensification period: early RI ($t = 90 \text{ h}$), middle (mid) RI ($t = 108 \text{ h}$), and late RI ($t = 126 \text{ h}$). The time slices represent the approximate intensification period quartiles prior to the TC attaining its maximum intensity (i.e., the 25th, 50th, and 75th percentiles for the intensification time period; see the vertical colored lines in Fig. 1 and horizontal lines in Fig. 2 for reference). Snapshots of the horizontal vortex structure are created for each time slice and shown in Fig. 3, where the radar reflectivity, asymmetric wind vectors, and dry PV are averaged over each of the three layers described in section 4a.

During the early RI time slice, the TC is characterized by an asymmetric distribution of cyclonic PV anomalies located radially inward of reflectivity maxima in the nascent eyewall region. The asymmetric wind circulation depicts pathways for air to be exchanged between the nascent eyewall and developing vortex eye, primarily in regions of relatively weaker convection. Transitioning 18 h later to the mid-RI time slice, the azimuthal distributions of PV and reflectivity have become increasingly axisymmetric and the TC is characterized by a high-PV annulus at each layer in its circulation; however, there remains a predominant $m = 3$ asymmetry in the low and middle layers of the vortex, characterized by convective maxima collocated with the vertices of the polygonal eyewall structure. Furthermore, asymmetric wind circulations associated with PV maxima embedded in the vertices of the polygonal eyewall continue to depict pathways for air to be exchanged between the eye and eyewall. Transitioning 18 h later to the late RI time slice, the azimuthal distributions of PV and convection have become concentrated in a highly asymmetric, elliptical eyewall structure extending throughout the depth of the vortex circulation. The low- and middle-layer asymmetric wind circulations depict a strong deformation zone within the inner-core region of the vortex; there is an axis of dilatation oriented azimuthally upwind of the ellipse

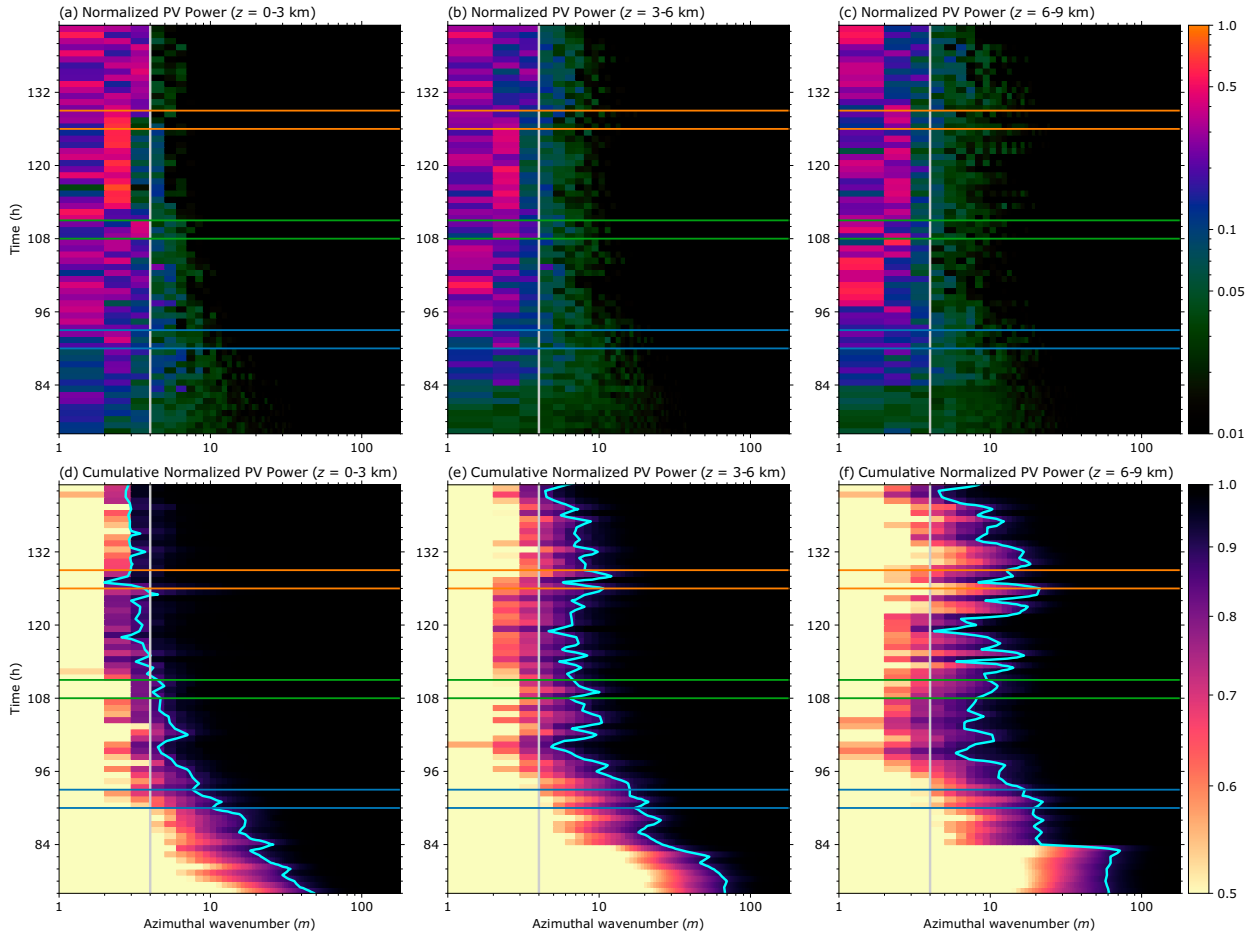


FIG. 2. (a)–(c) The inner-core PV normalized power spectra and (d)–(f) the inner-core PV cumulative normalized power spectra are shown as a function of azimuthal wavenumber m and time during the intensification period for (a),(d) the low layer ($z = 0\text{--}3 \text{ km}$), (b),(e) the midlayer ($z = 3\text{--}6 \text{ km}$), and (c),(f) the high layer ($z = 6\text{--}9 \text{ km}$). The cyan contour in (d)–(f) denotes 90% of the cumulative normalized power at each hourly time step. The horizontal, colored lines represent the three time windows analyzed during the intensification period: early RI (blue; $t = 90\text{--}93 \text{ h}$), mid-RI (green; $t = 108\text{--}111 \text{ h}$), and late RI (orange; $t = 126\text{--}129 \text{ h}$). The vertical gray line separates the low-wavenumber asymmetries ($m = 1\text{--}3$) from the high-wavenumber asymmetries ($m = 4\text{--}180$). The abscissa is left aligned such that the power for azimuthal wavenumber $m = 1$ is shaded between $m = 1\text{--}2$.

vertices and an axis of contraction oriented downwind of the ellipse vertices. Although the inner-core region of the vortex generally progresses toward increasing symmetricity throughout the intensification period (Fig. 1c), the snapshots presented in Fig. 3 further demonstrate that the magnitude of the asymmetries also increases throughout the intensification period.

c. Axisymmetric and asymmetric vortex structure

To assess both the axisymmetric and asymmetric evolution of the vortex structure, additional snapshots are created for each time slice from two perspectives (planes) within the vortex circulation: the radius–altitude (axisymmetric) plane (Fig. 4) and the radius–azimuth (top-down) plane (Figs. 5–7). The top-down plane is constructed by layer averaging quantities between the low ($z = 0\text{--}3 \text{ km}$) and high ($z = 6\text{--}9 \text{ km}$) layers.

During the early RI time slice ($t = 90 \text{ h}$), the overall vortex structure comprises a relatively weak-amplitude hollow PV tower superposed by convectively generated, cyclonic PV anomalies (Figs. 4a,d and 5). Note that the hollowness at a given vertical level is defined by the ratio of the eye to inner-core PV (e.g., Schubert et al. 1999; Hendricks et al. 2009), such that the hollowness parameter scales inversely with the relative magnitude of PV in the eyewall region. The axisymmetric vortex structure is characterized by a tangential (primary) circulation with an $\sim 35 \text{ m s}^{-1}$ near-surface maximum and a rapidly decaying vertical structure (Fig. 4a). Additionally, the transverse (secondary) circulation is characterized by boundary layer inflow exceeding 5 m s^{-1} near the surface, a modest eyewall updraft of $\sim 2 \text{ m s}^{-1}$ concentrated along the inner edge of the RMW, and upper-tropospheric radial outflow exceeding 10 m s^{-1} above 12-km altitude. The eyewall updraft is accompanied by a diabatic heating maximum of 20 K h^{-1} , and a hollow PV tower structure

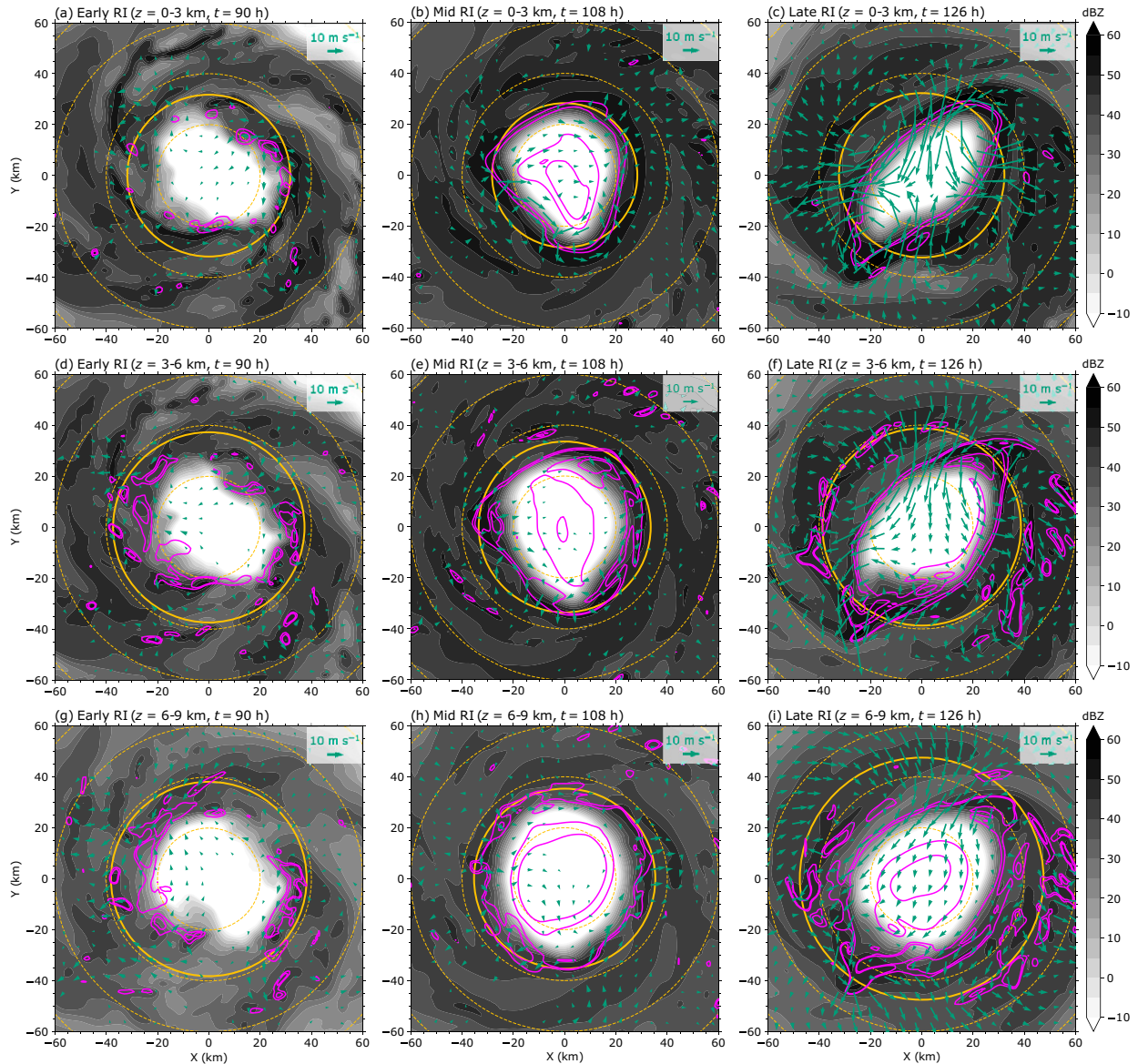


FIG. 3. The layer-averaged, inner-core vortex structure is shown for the (a),(d),(g) early RI time slice ($t = 90$ h), (b),(e),(h) the mid-RI time slice ($t = 108$ h), and (c),(f),(i) the late RI time slice ($t = 126$ h). (a)–(c) The low layer ($z = 0\text{--}3$ km), (d)–(f) the midlayer ($z = 3\text{--}6$ km), and (g)–(i) the high layer ($z = 6\text{--}9$ km). Radar reflectivity (shaded, dBZ) is overlaid with the asymmetric wind vectors (m s^{-1}), and the dry Ertel's PV is contoured in magenta at 20 and 30 PVU. The solid gold ring in each panel denotes the layer-averaged, azimuthal-mean RMW and dashed gold radius rings are shown in 20-km increments from the center.

has begun to emerge with maximum values of ~ 20 PVU ($1 \text{ PVU} = 10^{-6} \text{ K kg}^{-1} \text{ m}^2 \text{ s}^{-1}$) concentrated radially inward of the diabatic heating maximum (Fig. 4d). The asymmetric vortex structure is characterized by small-scale, convectively generated PV anomalies embedded within the inner-core vortex circulation (Fig. 5). There is a low-wavenumber $m = 2$ PV asymmetry superposed by high-wavenumber structures. Consistent with the inner-core PV spectral analysis (Fig. 2), the asymmetric PV distribution is concentrated among higher azimuthal wavenumbers (i.e., smaller azimuthal scales) with increasing altitude in the vortex circulation.

During the mid-RI time slice ($t = 108$ h), the overall vortex structure comprises a relatively strong-amplitude hollow PV tower superposed by a predominant $m = 3$ PV asymmetry (Figs. 4b,e and Fig. 6). The primary circulation has strengthened approximately twofold throughout the troposphere with an $\sim 70 \text{ m s}^{-1}$ near-surface maximum, while the magnitude of the secondary circulation has strengthened by a factor of ~ 4 (Fig. 4b). From the early to the mid-RI time slice, the RMW contracted approximately 5 km. The diabatic heating maximum remains concentrated along the inner edge of the RMW, exceeding 80 K h^{-1} , and the strengthened hollow PV

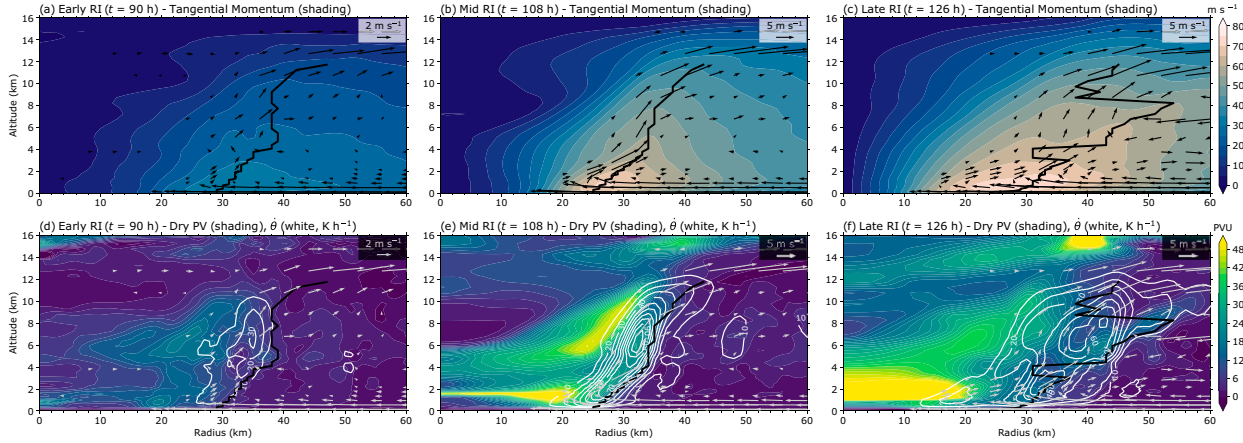


FIG. 4. The axisymmetric vortex structure is shown for (a),(d) the early RI time slice ($t = 90$ h), (b),(e) the mid-RI time slice ($t = 108$ h), and (c),(f) the late RI time slice ($t = 126$ h). (a)–(c) Tangential momentum (shaded, m s^{-1}) is overlaid with the transverse circulation (vectors, m s^{-1}). (d)–(f) The dry Ertel's potential vorticity (shaded, PVU) is overlaid with the transverse circulation (vectors, m s^{-1}) and diabatic heating from microphysical processes (white, contoured at 5, 10, 20, 40, 60, and 80 K h^{-1}). Transverse circulation vectors with a magnitude less than 0.5 m s^{-1} are excluded from (a) and (d), and transverse circulation vectors with a magnitude less than 1 m s^{-1} are excluded from (b), (c), (e), and (f). The black line in each panel denotes the azimuthal-mean RMW.

tower exhibits three distinct maxima: a primary maximum exceeding 60 PVU located between 1- and 2-km altitude along the low-layer PV bridge, a secondary maximum exceeding 50 PVU located along the midlayer PV bridge, and a tertiary maximum exceeding 45 PVU located in the upper-troposphere–lower-stratosphere (UTLS) region above the eyewall (Fig. 4e). The top-down analysis for the mid-RI time slice depicts a high-PV annulus structure in both the low and high layers (Fig. 6). Similar to the early RI time slice, the

predominant low-wavenumber $m = 3$ PV asymmetry is superposed by high-wavenumber structures. Furthermore, relatively high-amplitude PV asymmetries are present in the eyewall region with the same order of magnitude as the axisymmetric hollow PV tower.

During the late RI time slice ($t = 126$ h), the overall vortex structure comprises a more diffuse hollow PV tower compared to the mid-RI time slice and a highly asymmetric elliptical eyewall (Figs. 4c,f and 7). The primary circulation enveloping the

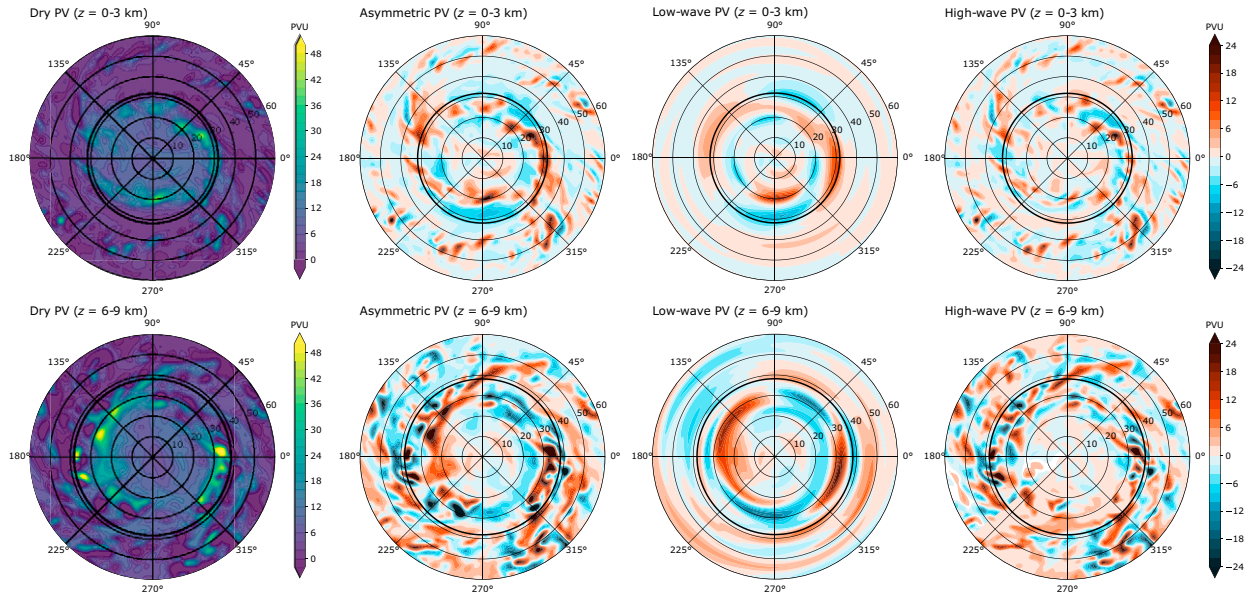


FIG. 5. The layer-averaged, dry Ertel's PV structure is shown for the early rapid intensification time slice ($t = 90$ h). (top) The low layer ($z = 0\text{--}3$ km) and (bottom) the high layer ($z = 6\text{--}9$ km). (from left to right) The dry Ertel's PV, the asymmetric PV, the low-wavenumber PV (azimuthal wavenumber $m = 1\text{--}3$), and the high-wavenumber PV ($m = 4\text{--}180$), respectively—all in PVU. The solid black ring in each panel denotes the layer-averaged, azimuthal-mean RMW.

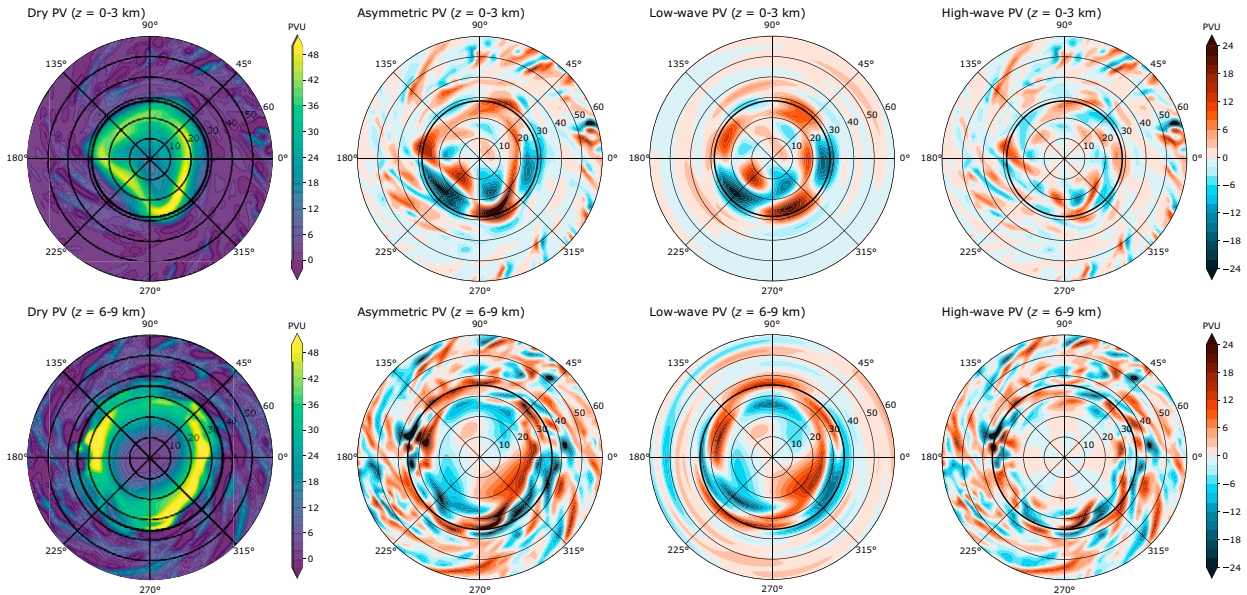


FIG. 6. As in Fig. 5, but for the mid-rapid intensification time slice ($t = 108$ h).

eyewall region has radially broadened—i.e., the radial gradients of tangential momentum have weakened—but the maximum tangential momentum remains above 70 m s^{-1} , and the radial branches of the transverse circulation have continued to strengthen. From the mid- to late RI time slice, the slope of the RMW has increased and a second inflow maximum has emerged between ~ 4 - and 8-km altitude. The diabatic heating maximum has maintained its amplitude of $\sim 80 \text{ K h}^{-1}$; however, both the axisymmetric diabatic heating and PV structure have radially broadened in contrast to the mid-RI time slice. The low-layer axisymmetric PV structure more closely resembles a

monopole, indicative of substantial mixing occurring between the eye and eyewall. The top-down analysis for the late RI time slice depicts a pronounced $m = 2$ elliptical eyewall structure in both the low and high layers (Fig. 7); however, the asymmetric PV is distributed among higher wavenumbers in the high layer. In summation, the axisymmetric vortex circulation strengthens throughout the intensification period while the asymmetric PV distribution becomes concentrated among lower azimuthal wavenumbers. The following section will further elucidate asymmetric contributions to TC intensification in light of the axisymmetric vortex structure during each of the time slices.

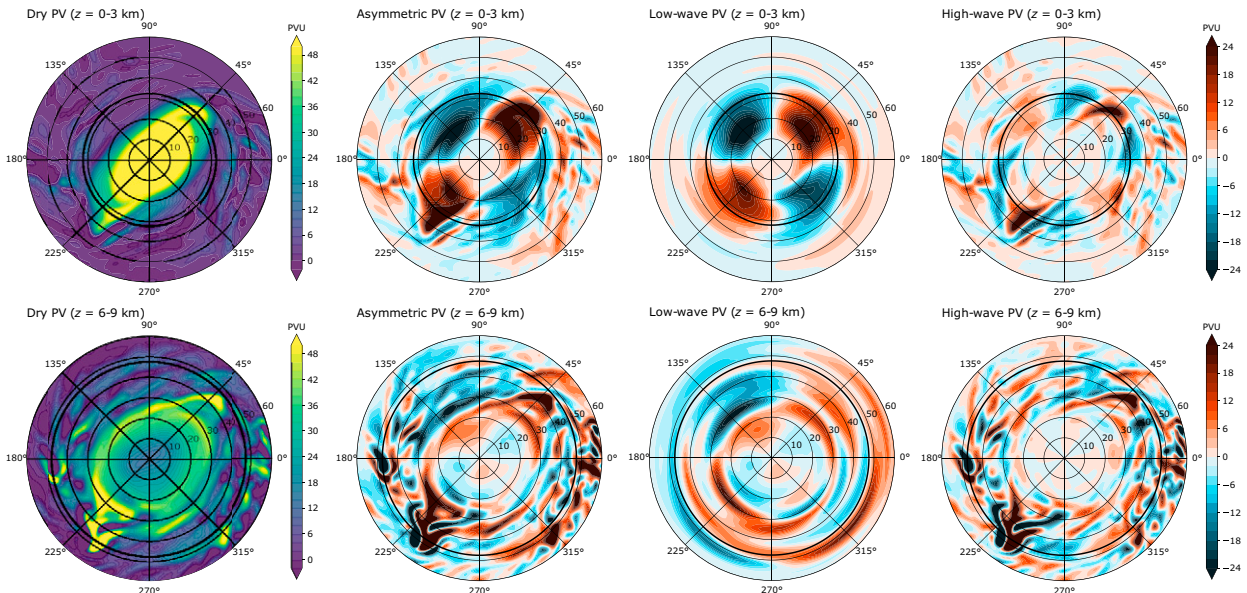


FIG. 7. As in Figs. 5 and 6, but for the late rapid intensification time slice ($t = 126$ h).

5. Scale-dependent contributions to intensification

The structural evolution of the vortex up to this point has been mostly discussed in context of the overall inner-core PV distribution. The flux form of the relative vorticity tendency (8) is chosen in lieu of the more complicated PV tendency as the flux form of the relative vorticity tendency does not feature the adiabatic/diabatic cancellation problem between the vertical PV advection and diabatic PV generation noted by [Tory et al. \(2012\)](#). The flux form of the relative vorticity tendency captures the principal dynamics contributing to the kinematic evolution of the vortex circulation and benefits from the conceptual simplicity of interpreting the flux divergence of a 2D vector. Furthermore, the product of the radius r and the absolute vorticity tendency can be integrated from the axis of rotation to a given radius and scaled by r^{-1} to produce the tangential momentum v tendency.

The contributions from axisymmetric, low-wavenumber, and high-wavenumber processes to both the azimuthal-mean relative vorticity $\bar{\zeta}$ and tangential momentum \bar{v} tendencies are analyzed for the three time slices during intensification. The simulation is restarted beginning at each of the time slices and model output is stored every five minutes for the proceeding 3-h time period. The objective is to elucidate how asymmetries contribute to the intensification process as the axisymmetric vortex structure continuously evolves. Therefore, the individual contributions to the $\bar{\zeta}$ and \bar{v} tendencies are summed for each wavenumber category (axisymmetric, low wavenumber, and high wavenumber), and results are presented in the context of scale-dependent contributions to the axisymmetric vortex intensification. The diffusive contributions from the subgrid-scale turbulence parameterization are included in the axisymmetric sum of contributions.

a. Early RI evolution

In the early stage of intensification ($t = 90\text{--}93$ h), the vortex evolution is primarily characterized by the aggregation of convectively generated, cyclonic vorticity anomalies, or “vorticity patches,” that long outlive their originating convective anomalies (e.g., [Wissmeier and Smith 2011](#)). To illustrate aspects of the general vortex evolution during the early RI time period, [Fig. 8](#) shows snapshots capturing the formation and evolution of a vorticity patch that contributes to the most salient low-wavenumber feature during the 3-h time period. A convectively generated vorticity patch begins to aggregate with a remnant vorticity patch that outlived its originating convection in the southern quadrant of the vortex. As the emergent vorticity patch rapidly expands in diameter, it becomes “wrapped up” in convection that develops a pronounced radial orientation and protrudes toward the center of the vortex. The vorticity patch subsequently becomes separated from its originating convection, spiraling toward the axis of rotation and producing a low-wavenumber radial dipole pattern in both the $\bar{\zeta}$ and \bar{v} tendencies that contributes to a substantial $\bar{\zeta}$ spinup of $\sim 15 \times 10^{-4} \text{ s}^{-1}$ and a \bar{v} spinup of $\sim 5\text{--}10 \text{ m s}^{-1}$ in a 30-min time window ([Figs. 9d](#) and [10d](#)). It remains unclear if the singular process described above is vital to the overall axisymmetric vortex intensification given its transient nature

relative to the full 67-h intensification period. There is a modest, but persistent axisymmetric contribution to the spinup of $\bar{\zeta}$ radially inward of the RMW and near the $\bar{\zeta}$ maximum in association with the nascent eyewall ([Fig. 9a](#)). The axisymmetric contributions also persistently spin up \bar{v} along the RMW between 1 and $2 \text{ m s}^{-1} \text{ h}^{-1}$ throughout the early RI time period ([Fig. 10a](#)). In contrast, the high-wavenumber contributions have a relatively weak magnitude, but they are on average characterized by a radial dipole pattern that spins up $\bar{\zeta}$ and \bar{v} approximately 10 km radially inward of the RMW and spins down both quantities near the RMW ([Figs. 9g](#) and [10g](#)).

The evolution noted during early RI is akin to the successive aggregation and upscale growth of cyclonic vorticity anomalies inherent to tropical cyclogenesis ([Hendricks et al. 2004; Montgomery et al. 2006, 2012](#)). The analyses presented in [Figs. 3](#) and [5](#) revealed that the overall vortex structure is best characterized by cyclonic vorticity anomalies distributed throughout the nascent TC eyewall rather than an axisymmetric annulus of high-vorticity air, such that the axisymmetric vortex structure is largely a product of averaging numerous cyclonic vorticity anomalies ([Persing et al. 2013; Montgomery et al. 2021](#)). Therefore, the transverse circulation is supported by convective anomalies and their associated boundary layer convergence, producing net azimuthal-mean ascent in the nascent TC eyewall. However, [Figs. 9a](#) and [10a](#) demonstrate it is the contribution from the convective anomalies that collectively projects onto the axisymmetric processes that is paramount to TC intensification (e.g., [Nolan and Grasso 2003; Nolan et al. 2007](#)).

b. Mid-RI evolution

In the midstage of intensification ($t = 108\text{--}111$ h), the high-PV annulus along the inner edge of the eyewall is characterized by a predominant $m = 3$ PV asymmetry ([Fig. 6](#)). As the $m = 3$ PV asymmetry orbits the vortex circulation, it produces undulations in the structure of the high-PV annulus with an approximate period of the local vortex circulation (~ 45 at the RMW). The undulations are accompanied by “pulsing cycles” where the low-layer $\bar{\zeta}$ annulus exhibits transient maxima followed by low-wavenumber features that propagate radially inward toward the axis of rotation ([Figs. 9b,e,h](#)). The axisymmetric contributions to the $\bar{\zeta}$ tendency are primarily characterized by a spinup tendency located along the radially outward flank of the high-vorticity annulus, and the spinup tendency is straddled by spindown tendencies ([Fig. 9b](#)). Given that the axisymmetric $\bar{\zeta}$ spindown tendencies are concentrated along the flanks of the vorticity annulus, the axisymmetric processes are directly contributing to amplifying the $\bar{\zeta}$ annulus and decreasing the hollowness parameter. The axisymmetric contributions to the \bar{v} tendency are characterized by a persistent radial “spinup dipole” pattern, with a spinup tendency concentrated along the RMW and a spindown tendency concentrated radially inward of the RMW ([Figs. 10b,k](#)). The location of the radial spinup dipole pattern further indicates that the axisymmetric processes are directly facilitating the development of a “U-shaped” tangential wind profile ($\partial^2 \bar{v} / \partial r^2 > 0$; [Kossin and Schubert 2001](#)).

As the eyewall structure undulates, vorticity is shed from the $\bar{\zeta}$ annulus and transported toward the axis of rotation via

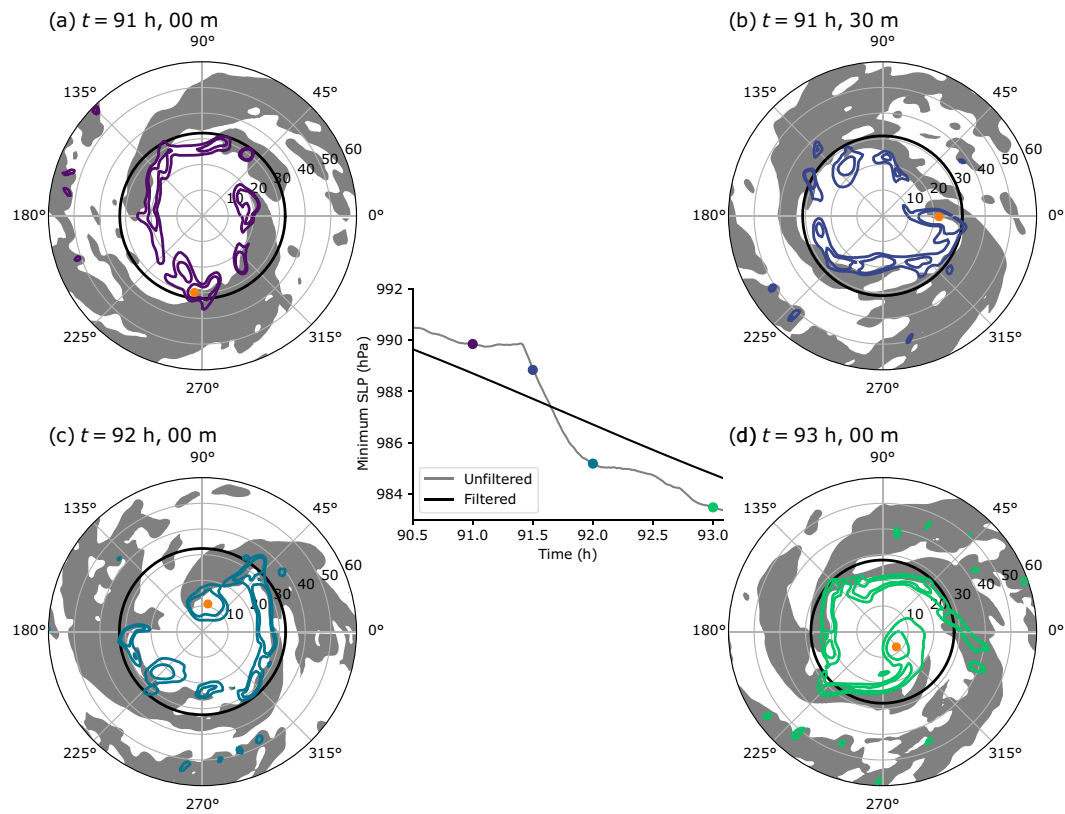


FIG. 8. (center) The minimum sea level pressure (SLP; hPa) time series is shown for a portion of the early RI time period ($t = 90.5\text{--}93 \text{ h}$) using 1-min model output (gray) and overlaid with its smoothed time series using a 12-h Lanczos filter with 361 weights (black). The colored dots correspond to snapshots taken at different times throughout the early RI time period, given by the titles in each panel. (a)–(d) Radar reflectivity (dBZ) at 1-km altitude is shaded in gray for values greater than 35 dBZ. The low-layer-averaged ($z = 0\text{--}3 \text{ km}$) relative vorticity is contoured at 30 and $40 \times 10^{-4} \text{ s}^{-1}$, and the contour colors correspond to the colored dots in the center panel. The solid black ring in each panel denotes the low-layer-averaged, azimuthal-mean RMW. The orange dot in each panel denotes the location of the cyclonic relative vorticity maximum associated with the vorticity patch discussed in section 5a.

low-wavenumber processes (Figs. 9e,k). The low-wavenumber contributions to the \bar{v} tendency are primarily characterized by a radial “spindown dipole” pattern that opposes the axisymmetric contributions, with a spindown tendency concentrated along the RMW and a spinup tendency concentrated radially inward of the RMW (Figs. 10e,k). The high-wavenumber contributions to the $\bar{\zeta}$ and \bar{v} tendencies exhibit similar radial patterns to their low-wavenumber counterparts, and also appear to evolve together with the aforementioned pulsing cycles; however, the high-wavenumber contributions have a relatively weaker magnitude than the low-wavenumber contributions and mostly do not exhibit radially propagating features.

The eyewall undulations and pulsing cycles are surmised to be enveloped by a relatively low-frequency vacillation cycle given the progression of the axisymmetric vortex structure toward a $\bar{\zeta}$ monopole at the end of the mid-RI time period (Figs. 9b,e,h). Collectively, the results demonstrate that the vacillation cycles described in previous studies (e.g., Nguyen et al. 2011; Hankinson et al. 2014; Hardy et al. 2021) might further comprise relatively high-frequency oscillations denoted pulsing

cycles herein given that their frequency matches the pulse—i.e., period—of the local vortex circulation. Furthermore, the combined pulsing and vacillation cycles characterizing the eyewall evolution are posited to initiate the relative slowdown in the evolution of the vortex circulation discussed earlier in section 4a, beginning with an $\sim 6\text{-h}$ intensification break that commences near the start of mid-RI (Fig. 1). Thus, the pulsing cycles impede the intensification process via undulations that shed vorticity from the $\bar{\zeta}$ annulus akin to the vacillation cycles impeding the intensification process via eye–eyewall mixing that transitions the $\bar{\zeta}$ annulus to a monopole. A more comprehensive assessment of how the combined pulsing and vacillation cycles contribute to the intensification process would entail the non-linear contributions from the structural rearrangement of the axisymmetric vortex circulation brought about by the wave–mean flow interactions.

c. Late RI evolution

In the late stage of intensification, the inner-core vortex structure is highly asymmetric and characterized by a predominant

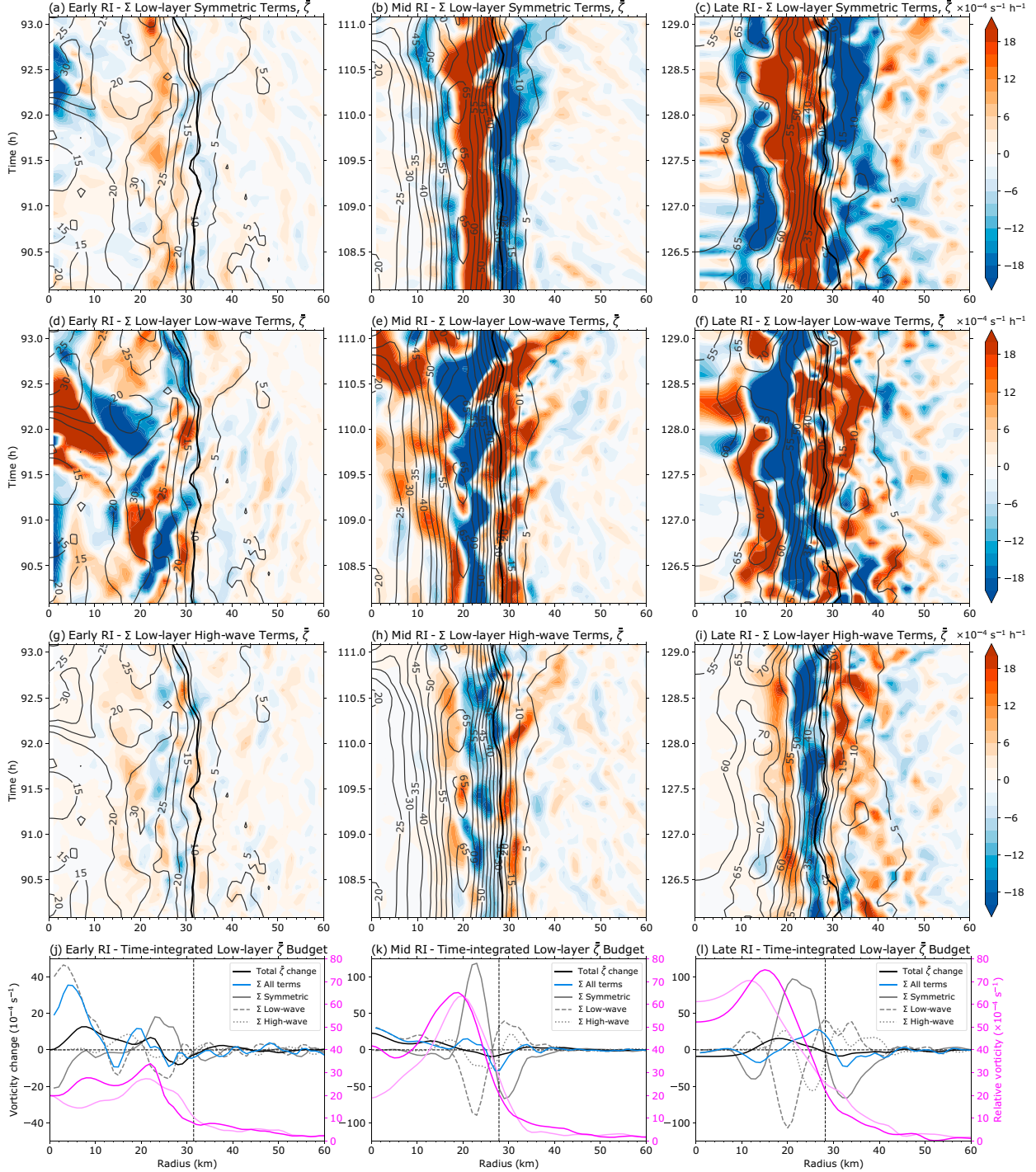


FIG. 9. Low-layer-averaged ($z = 0\text{--}3 \text{ km}$) scale-dependent contributions to the azimuthal-mean relative vorticity $\bar{\zeta}$ budget (shaded, $\times 10^{-4} \text{ s}^{-1} \text{ h}^{-1}$) are shown as a function of radius and time for (a),(d),(g) the early RI time period ($t = 90\text{--}93 \text{ h}$), (b),(e),(h) the mid-RI time period ($t = 108\text{--}111 \text{ h}$), and (c),(f),(i) the late RI time period ($t = 126\text{--}129 \text{ h}$). (a)-(c) The axisymmetric contributions to the $\bar{\zeta}$ budget, (d)-(f) the low-wavenumber contributions, and (g)-(i) the high-wavenumber contributions. The thin black contours denote $\bar{\zeta}$ contoured every $5 \times 10^{-4} \text{ s}^{-1}$, and the thick black contour denotes the layer-averaged, azimuthal-mean RMW. (j)-(l) The time-integrated contributions for each respective 3-h time period ($\times 10^{-4} \text{ s}^{-1}$) shown in (a)-(i), overlaid with $\bar{\zeta}$ ($\times 10^{-4} \text{ s}^{-1}$) at the start (light magenta) and end (dark magenta) of each respective 3-h time period. The vertical dashed lines in (j)-(l) denote the RMW averaged over each time period.

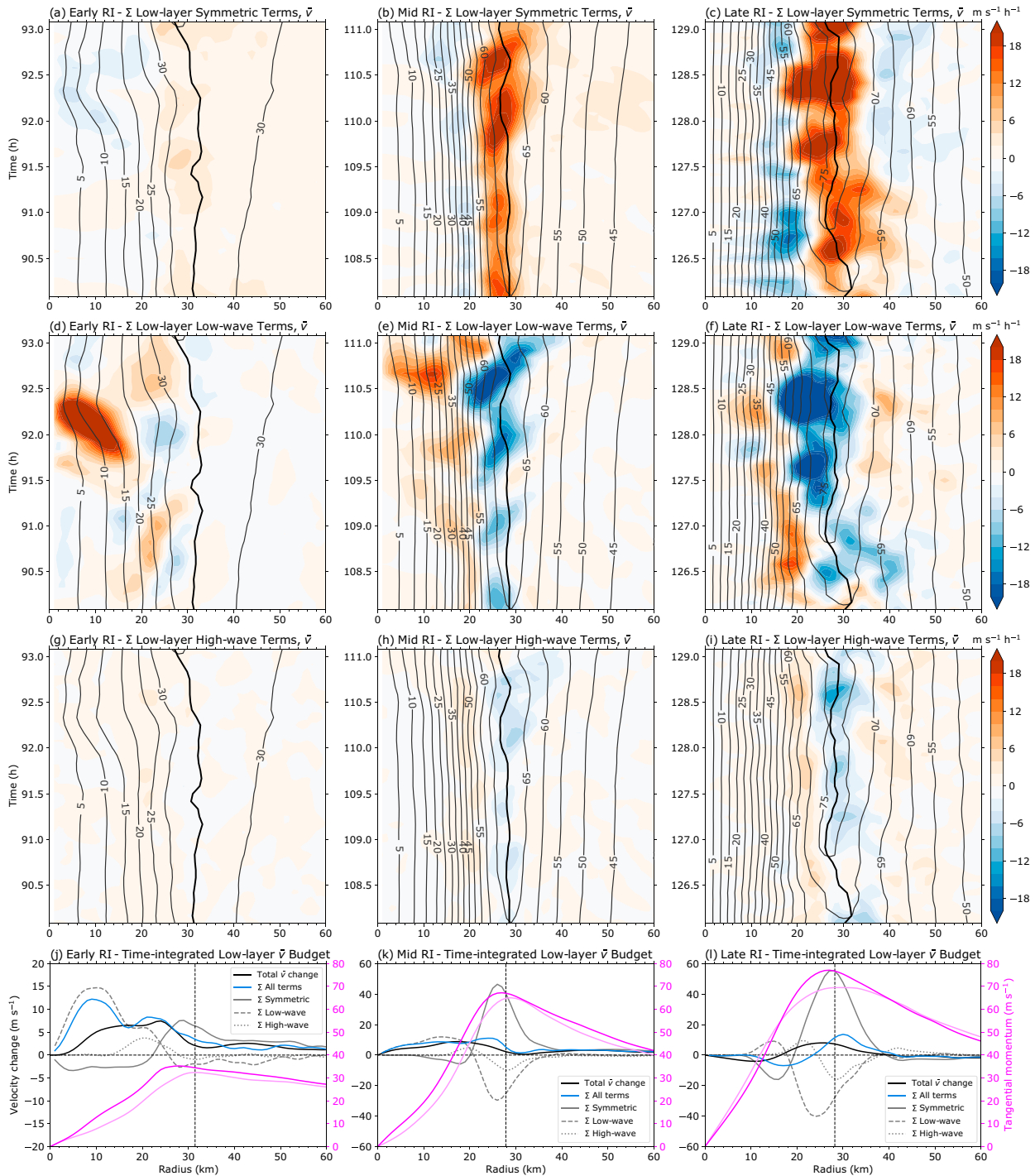


FIG. 10. Low-layer-averaged ($z = 0\text{--}3 \text{ km}$) scale-dependent contributions to the azimuthal-mean tangential momentum \bar{v} budget (shaded, $\text{m s}^{-1} \text{h}^{-1}$) are shown as a function of radius and time for (a),(d),(g) the early RI time period ($t = 90\text{--}93 \text{ h}$), (b),(e),(h) the mid-RI time period ($t = 108\text{--}111 \text{ h}$), and (c),(f),(i) the late RI time period ($t = 126\text{--}129 \text{ h}$). (a)–(c) The axisymmetric contributions to the \bar{v} budget, (d)–(f) the low-wavenumber contributions, and (g)–(i) the high-wavenumber contributions. The thin black contours denote the layer-averaged, azimuthal-mean tangential momentum contoured every 5 m s^{-1} , and the thick black contour denotes the layer-averaged, azimuthal-mean RMW. (j)–(l) The time-integrated contributions for each respective 3-h time period (m s^{-1}) shown in (a)–(i), overlaid with \bar{v} (m s^{-1}) at the start (light magenta) and end (dark magenta) of each respective 3-h time period. The vertical dashed lines in (j)–(l) denote the RMW averaged over each time period.

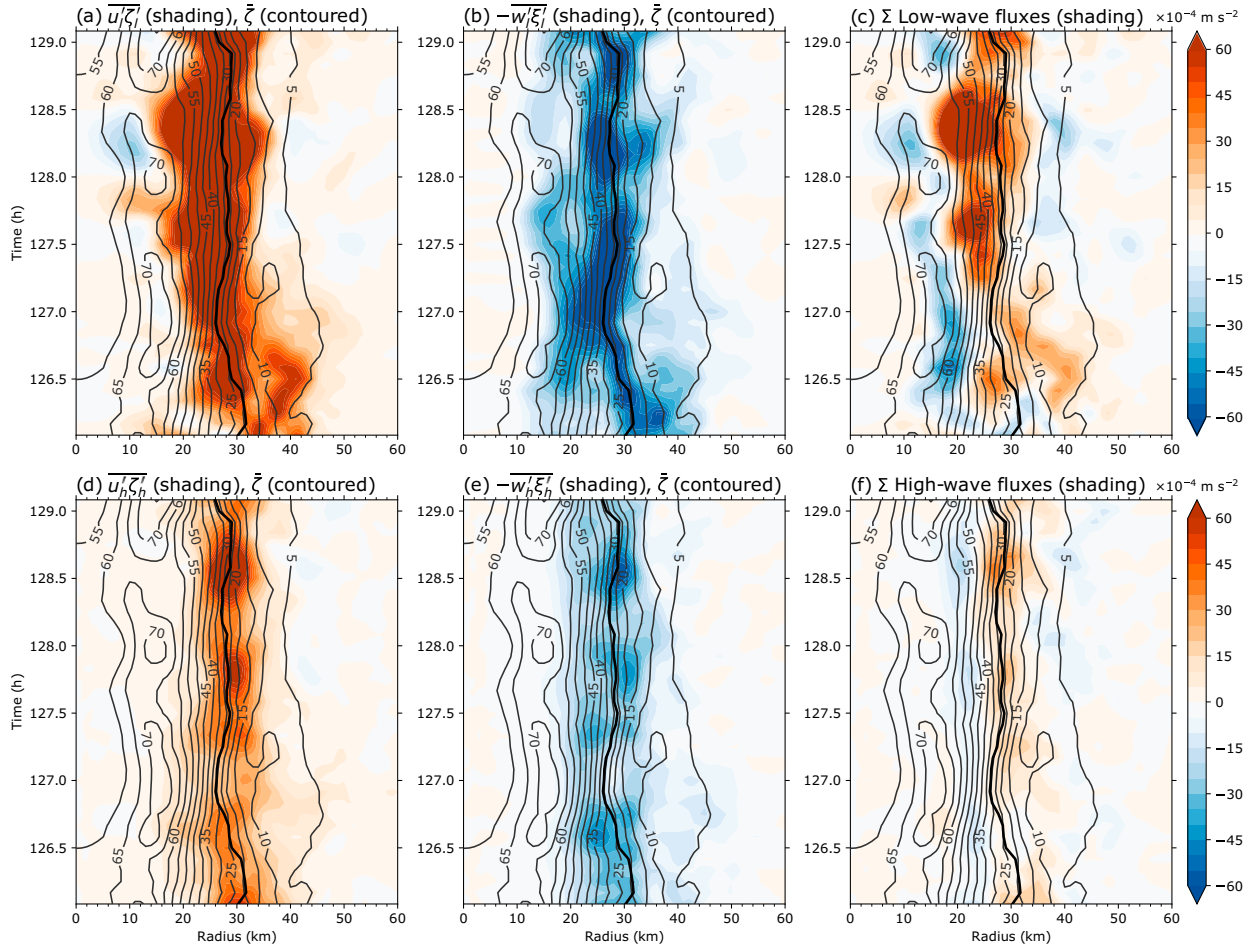


FIG. 11. (a),(d) The low-layer-averaged ($z = 0$ –3 km), advective fluxes ($\bar{u}'\zeta'$), (b),(e) nonadvective fluxes ($-\bar{w}'\xi'$), and (c),(f) the sum of both the advective and nonadvective fluxes are shown as a function of radius and time (shaded, $\times 10^{-4} \text{ m s}^{-2}$) for the late RI time period ($t = 126$ –129 h). (a)–(c) The low-wavenumber fluxes and (d)–(f) the high-wavenumber fluxes. Negative values represent a radially inward-directed flux and positive values represent a radially outward-directed flux. See (7) for details regarding the fluxes as defined within the flux form of the relative vorticity tendency. The thin black contours denote the layer-averaged, azimuthal-mean relative vorticity contoured every $5 \times 10^{-4} \text{ s}^{-1}$, and the thick black contour denotes the layer-averaged, azimuthal-mean RMW.

azimuthal wavenumber $m = 2$ elliptical eyewall (Fig. 7). There is an $m = 2$ VRW retrograding relative to the local angular flow along the waveguide of an approximate PV monopole, with an azimuthal phase velocity that matches the value predicted in linear, barotropic wave theory. To illustrate the dynamical processes accompanying the $m = 2$ VRW, Fig. 11 shows a partitioning of the low- and high-wavenumber contributions to the $\bar{\zeta}$ tendency into the advective flux $\bar{u}'\zeta'$ and nonadvective flux² $-\bar{w}'\xi'$. Although it is the divergence of each flux that contributes to the $\bar{\zeta}$ tendency (8), the low- and high-wavenumber fluxes provide additional insight toward understanding the nature of

asymmetric processes accompanying the $m = 2$ VRW. The low-wavenumber, advective processes accompanying the $m = 2$ VRW primarily contribute to a downgradient flux of relative vorticity away from the low-layer $\bar{\zeta}$ maximum located between 10- and 15-km radius (Fig. 11a). In contrast, the low-wavenumber, nonadvective processes contribute to an upgradient flux of relative vorticity from near the RMW toward the low-layer $\bar{\zeta}$ maximum (Fig. 11b). The nonadvective, upgradient flux arises from the convective coupling of the $m = 2$ VRW—the radial vorticity anomalies are collocated (in-azimuthal phase) with like-signed vertical velocity anomalies such that their product yields an inward directed (negative) flux along the negative radial gradient of relative vorticity.

The low-wavenumber, nonadvective upgradient flux cooperates with the axisymmetric circulation to regenerate the low-layer, hollow $\bar{\zeta}$ annulus structure between \sim 20- and 25-km radius (see Figs. 9c,l and 11b), but the low-wavenumber,

² For brevity, the terminology distinguishing between advective and nonadvective processes introduced by Haynes and McIntyre (1987) is adapted herein for the flux form of the relative vorticity tendency in geometric coordinates (7) and (8); however, the nomenclature was originally introduced for the flux form of the potential vorticity substance tendency in isentropic coordinates.

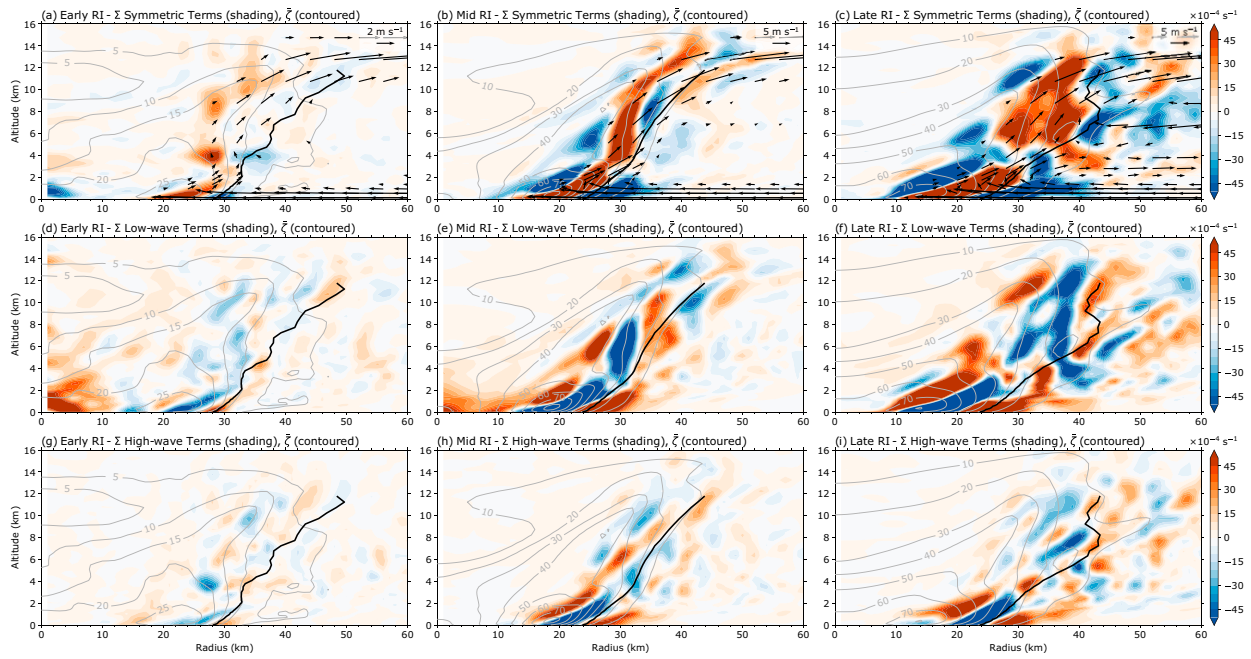


FIG. 12. The time-integrated, scale-dependent contributions to the azimuthal-mean relative vorticity $\bar{\zeta}$ budget (shaded, $\times 10^{-4} \text{ s}^{-1}$) are shown as a function of radius and altitude for the (a),(d),(g) early RI time period ($t = 90\text{--}93 \text{ h}$), (b),(e),(h) mid-RI time period ($t = 108\text{--}111 \text{ h}$), and (c),(f),(i) late RI time period ($t = 126\text{--}129 \text{ h}$). (a)–(c) Axisymmetric contributions to the $\bar{\zeta}$ budget, (d)–(f) low-wavenumber contributions, and (g)–(i) high-wavenumber contributions. The axisymmetric contributions are overlaid with the transverse circulation vectors averaged over each respective 3-h time period. Transverse circulation vectors with a magnitude less than 0.5 m s^{-1} are excluded from (a), and transverse circulation vectors with a magnitude less than 1 m s^{-1} are excluded from (b) and (c). The thin gray contours denote $\bar{\zeta}$ (contoured every 10^{-4} s^{-1}), and the thick black contour denotes the azimuthal-mean RMW, with both quantities averaged over each respective 3-h time period.

advective downgradient flux overwhelms the nonadvective upgradient fluxes on the radially outward flank of the $\bar{\zeta}$ annulus (Figs. 11a–c). The discrepancy between the magnitudes of the low-wavenumber vorticity fluxes partly arises from the relative magnitudes of the low-wavenumber vertical and radial velocities. The low-wavenumber vertical velocity is on average one order of magnitude smaller than the low-wavenumber radial velocity within the area confined by the low-layer RMW (not shown). Furthermore, the radial extent of the vertical velocity anomalies is smaller than the radial extent of the radial velocity anomalies given that the bulk of the updraft anomalies is confined to a narrow radial region within the elliptical eyewall. Despite the presence of substantive upgradient fluxes via low-wavenumber, nonadvective processes, the combined divergence of both the low-wavenumber, advective and nonadvective fluxes yields a spinup of $\bar{\zeta}$ along the low-layer $\bar{\zeta}$ annulus and a spindown along its radially outward flank (Fig. 9f). The advective and nonadvective vorticity fluxes are equivalent to the radial asymmetric vorticity flux and the vertical asymmetric advection of tangential momentum in the \bar{v} tendency, respectively, except that the signs of the asymmetric vorticity fluxes are by design opposite to their respective contributions in the \bar{v} tendency (cf. Figs. 11c and 10f; cf. Figs. 11f and 10i). Therefore, the aforementioned dominance of the advective, downgradient vorticity fluxes relative to the nonadvective, upgradient vorticity fluxes directly contributes to

the radial spindown dipole pattern noted in the \bar{v} tendency (Figs. 10f,i,l), such that the convectively coupled $m = 2$ VRW is impeding axisymmetric vortex intensification during the late RI time period. The high-wavenumber contributions to the $\bar{\zeta}$ and \bar{v} tendencies again exhibit similar radial patterns to their low-wavenumber counterparts but with relatively weaker magnitudes and displaced further radially outward (Figs. 9i and 10i).

The low- and high-wavenumber, radial fluxes of tangential momentum $\bar{u}'\bar{v}'$ also exhibit upgradient characteristics along the inner edge of the RMW during the intensification period (not shown). Persing et al. (2013) noted similar upgradient fluxes of tangential momentum from the resolved asymmetric processes in their idealized, 3D simulation of a stationary TC, and the findings presented herein corroborate the authors' statement that the resolved asymmetric fluxes of tangential momentum are thus not solely diffusive. However, the divergence of the tangential momentum fluxes integrated throughout each of the respective intensification time periods indicates that the upgradient fluxes of tangential momentum via asymmetric processes contribute to a radial spindown dipole pattern in the \bar{v} tendency.

d. Azimuthal-mean tendencies

To assess variability in the vertical structure of scale-dependent contributions to the azimuthal-mean vortex evolution, Figs. 12 and 13 show azimuthal-mean cross sections of

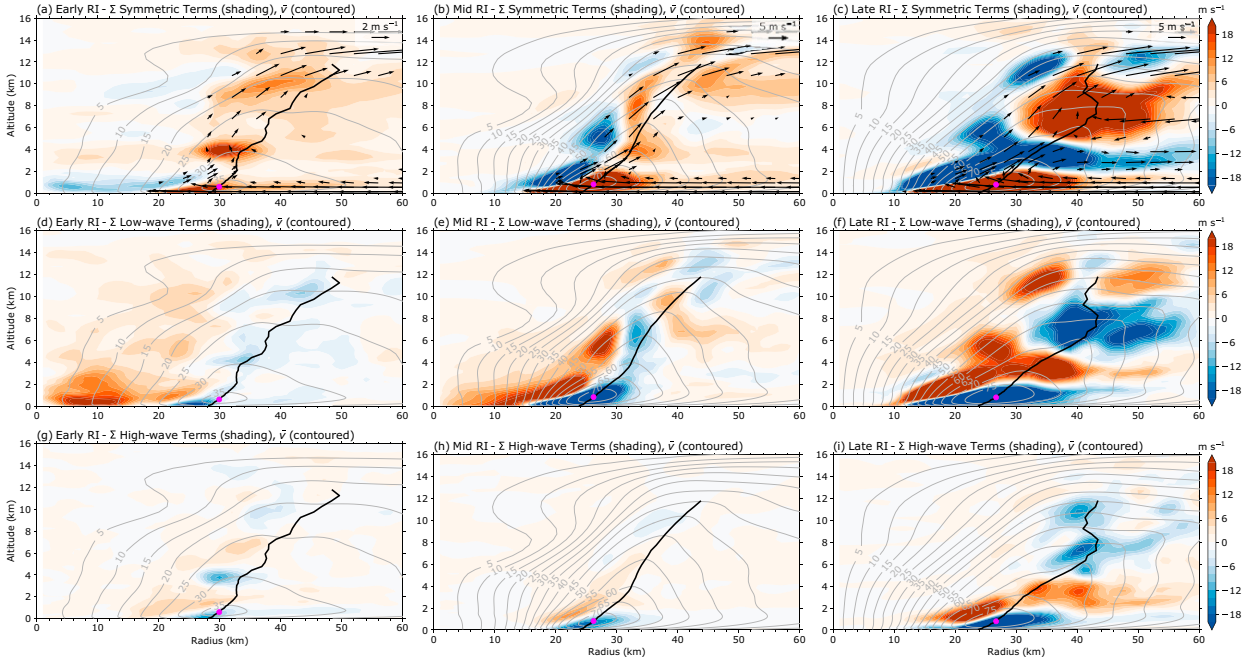


FIG. 13. The time-integrated, scale-dependent contributions to the azimuthal-mean tangential momentum \bar{v} budget (shaded, $\times 10^{-4} \text{ s}^{-1}$) are shown as a function of radius and altitude for the (a),(d),(g) early RI time period ($t = 90\text{--}93 \text{ h}$), (b),(e),(h) mid-RI time period ($t = 108\text{--}111 \text{ h}$), and (c),(f),(i) late RI time period ($t = 126\text{--}129 \text{ h}$). (a)-(c) Axisymmetric contributions to the \bar{v} budget, (d)-(f) low-wavenumber contributions and (g)-(i) high-wavenumber contributions. The axisymmetric contributions are overlaid with the transverse circulation vectors averaged over each respective 3-h time period. Transverse circulation vectors with a magnitude less than 0.5 m s^{-1} are excluded from (a), and transverse circulation vectors with a magnitude less than 1 m s^{-1} are excluded from (b) and (c). The thin gray contours denote \bar{v} (contoured every 5 m s^{-1}), and the thick black contour denotes the azimuthal-mean RMW, with both quantities averaged over each respective 3-h time period. The magenta dot in each panel denotes the time-averaged location of the maximum \bar{v} .

the net (temporally integrated) scale-dependent contributions to the $\bar{\zeta}$ and \bar{v} tendencies integrated over each 3-h intensification time period, respectively. Consistent with the low-layer analyses presented in Figs. 9 and 10, the axisymmetric contributions to the $\bar{\zeta}$ tendency are characterized by a spinup tendency concentrated along the radially outward flank of the hollow vorticity tower that approximately follows the slope of the RMW with increasing altitude, and the spinup tendency is straddled by spindown tendencies (Figs. 12a–c). In contrast, the low- and high-wavenumber contributions to the $\bar{\zeta}$ tendency largely oppose the axisymmetric contributions, especially within the lowest 4 km of the vortex circulation, but exhibit more variability relative to the axisymmetric contributions throughout the depth of the troposphere (Figs. 12d–i).

Overall, the axisymmetric processes contribute to a net spinup of \bar{v} along the RMW and throughout the troposphere of the vortex circulation, with an exception between approximately 2–5-km altitude during the late RI time period (Figs. 13a–c). In contrast, the low-wavenumber contributions to the \bar{v} tendency are primarily characterized by the aforementioned radial spindown dipole pattern that approximately follows the slope of the RMW with increasing altitude, with an exception between 2- and 5-km altitude during the late RI time period. To further assess the symmetric and low-wavenumber contributions along the RMW between 2- and 5-km altitude during the late RI time period,

the scale-dependent contributions to the tangential momentum tendency were further partitioned into their constituent radial and vertical advection contributions. The symmetric, radial advection of tangential momentum contributes to a spindown \bar{v} along the RMW between 2- and 5-km altitude, as indicated by the development of a symmetric radial outflow channel in the corresponding layer (Fig. 13c). In contrast, the low-wavenumber, vertical advection of tangential momentum dominates the low-wavenumber, radial advection of tangential momentum along the RMW between 2- and 5-km altitude (not shown), indicating that the low-wavenumber convective processes accompanying the $m = 2$ elliptical eyewall structure are facilitating vortex spinup between 2- and 5-km altitude during the late RI time period. Throughout the intensification period, the high-wavenumber contributions to the \bar{v} tendency exhibit a radial spindown dipole pattern in the boundary layer of the vortex circulation with relatively weaker magnitudes compared to the low-wavenumber contributions. There is an exception to the radial spindown dipole pattern where the high-wavenumber processes contribute to a modest, net spinup of \bar{v} in a shallow, approximately 2-km layer above the boundary layer throughout the intensification period (Figs. 13g–i). Collectively, the exceptions to the radial spindown dipole pattern—noted for the low-wavenumber processes between 2- and 5-km altitude during the late RI period and for the high-wavenumber processes

in a shallow, 2-km layer above the boundary layer throughout the intensification period—indicate that eyewall asymmetries can simultaneously contribute to a spinup of \bar{v} above the boundary layer while contributing to a spindown of \bar{v} within the boundary layer. Despite the aforementioned exceptions, the \bar{v} maximum resides in the boundary layer below 1-km altitude during each stage of the intensification process, as denoted by the magenta dots in Fig. 13. The contributions from asymmetric processes to the \bar{v} tendency are generally maximized below 2-km altitude—in the region of the \bar{v} maximum—and characterized by a radial spindown dipole pattern in this layer (Figs. 13d–i). Therefore, the asymmetric processes are primarily impeding the intensification process.

6. Concluding remarks

In an idealized, high-resolution simulation of a tropical cyclone (TC) intensifying while translating in uniform flow, eyewall asymmetries are found to generally impede the intensification process. During the intensification period, the asymmetric potential vorticity (PV) distribution progresses from numerous cyclonic PV anomalies that collectively constitute the nascent eyewall, to a predominant azimuthal wavenumber $m = 3$ PV asymmetry superposed on a high-PV annulus and undulating with a period matching the local vortex circulation, and then to an elliptical eyewall structure associated with a predominant $m = 2$ vortex Rossby wave (VRW) retrograding along the waveguide of an approximate PV monopole. The inner-core asymmetric PV distribution progresses toward lower azimuthal wavenumbers (i.e., larger azimuthal scales) throughout the intensification period while the overall vortex circulation progresses toward axisymmetry; however, axisymmetry is never attained during the intensification period.

The most prevalent pattern of asymmetric contributions to the axisymmetric tangential momentum \bar{v} tendency is characterized by a radial “spindown dipole,” whereby asymmetric processes spin down \bar{v} along the radius of maximum tangential winds (RMW) and spin up \bar{v} radially inward of the RMW. On the contrary, the most prevalent pattern of axisymmetric contributions to the \bar{v} tendency is characterized by a radial “spinup dipole,” whereby axisymmetric processes spin up \bar{v} along the RMW and spin down \bar{v} radially inward of the RMW. The magnitudes of the two radial dipoles largely oppose each other during the intensification period, but there is a small residual in favor of the axisymmetric processes and thus the vortex intensifies. Collectively, the asymmetric processes therefore impede intensification and radially broaden the axisymmetric vortex structure, while the axisymmetric processes directly facilitate intensification and aid the amplification of a hollow vorticity tower and its concomitant “U-shaped” tangential wind profile radially inward of the RMW. The radial spindown dipole pattern associated with asymmetric processes is evident among simulations with varying degrees of complexity and can be deduced from analyses in several previous studies. For example, PV mixing brought about by the release of barotropic instability is characterized by a radial spindown dipole pattern (e.g., Schubert et al. 1999;

Kossin and Eastin 2001; Hendricks et al. 2009; Hendricks and Schubert 2010), as are the wave–mean flow interactions in a linearized, 3D framework (e.g., Nolan and Grasso 2003; Nolan et al. 2007), and the wave–mean flow interactions in 3D frameworks that incorporate fully nonlinear, moist convective processes (e.g., Yang et al. 2007; Persing et al. 2013; Hardy et al. 2021; Montgomery et al. 2021). The most salient exception to the radial spindown dipole pattern associated with asymmetric contributions to the \bar{v} tendency occurs in a shallow, approximately 2-km layer above the boundary layer where high-wavenumber processes ($m > 3$) contribute to a modest spinup of \bar{v} along the RMW for each stage of the intensification period. Despite the variable nature of asymmetries throughout the intensification period for the vortex analyzed herein, the asymmetric processes are found to primarily oppose the axisymmetric processes and impede axisymmetric vortex intensification.

The asymmetric processes radially broaden the axisymmetric vortex structure throughout the intensification period, and this restructuring may have nonlinear ramifications for intensification through the balanced transverse circulation (Schubert and Hack 1982; Shapiro and Willoughby 1982; Hack and Schubert 1986; Pendergrass and Willoughby 2009; Schubert and McNoldy 2010) and wave–mean flow interactions (e.g., Hendricks and Schubert 2010). Balachandran et al. (2020) demonstrated that the growth of asymmetries can occur largely independent from the axisymmetric vortex, and therefore eddies do not necessarily grow at the expense of the mean. Although the possibility of asymmetries growing via wave–wave interactions cannot be discarded without further investigation, the foregoing discussion suggests that any eventual wave–mean flow interactions would primarily be characterized by spindown tendencies along the RMW. Additional research is required to verify the extent to which the asymmetries analyzed herein are growing through wave–wave interactions, and whether the nature of asymmetric contributions to the intensification process might be altered by concurrent wave–wave and wave–mean flow interactions.

Considerations should be made toward investigating how the origin and evolution of TC eyewall asymmetries might vary together with the axisymmetric vortex and its ambient environment. Potential avenues for future work could begin with testing the sensitivity of the predominant asymmetries to the boundary layer and microphysics parameterizations and the presence of vertical shear flow. The analyses presented herein alluded to eyewall asymmetries as convectively coupled features during various stages of evolution, suggesting that the origin and evolution of eyewall asymmetries might be sensitive to the fluxes of enthalpy and momentum occurring near the ocean surface and the subsequent release of latent heat within the TC eyewall. An idealized, ensemble-modeling framework could provide additional insight toward elucidating asymmetric contributions to TC intensification.

Acknowledgments. This material is based upon work supported by the National Center for Atmospheric Research, which is a major facility sponsored by the National Science

Foundation under Cooperative Agreement 1852977. This work was also supported by the Office of Naval Research Awards N000141613033 and N000142012069 and the National Science Foundation Award AGS-1701225. JM was also supported by the National Science Foundation Bridge to the Doctorate Fellowship Award 004863-00003. We acknowledge high-performance computing support from Cheyenne (doi:10.5065/D6RX99HX) provided by NCAR's Computational and Information Systems Laboratory, sponsored by the National Science Foundation.

Data availability statement. The model output from the high-resolution numerical simulation is too large to feasibly transfer or archive in an online repository. The simulation can be reproduced with the Cloud Model 1 (CM1) version 19.7 (<https://www2.mmm.ucar.edu/people/bryan/cm1/cm1r19.7.tar.gz>). Files containing the model initial conditions, namelist settings, environmental sounding, and large-scale wind nudging are available via the Zenodo repository located at <https://doi.org/10.5281/zenodo.5655635>.

REFERENCES

- Alland, J. A., B. H. Tang, K. L. Corbosiero, and G. H. Bryan, 2021: Combined effects of midlevel dry air and vertical wind shear on tropical cyclone development. Part I: Downdraft ventilation. *J. Atmos. Sci.*, **78**, 763–782, <https://doi.org/10.1175/JAS-D-20-0054.1>.
- Bell, M. M., and M. T. Montgomery, 2008: Observed structure, evolution, and potential intensity of category 5 Hurricane Isabel (2003) from 12 to 14 September. *Mon. Wea. Rev.*, **136**, 2023–2046, <https://doi.org/10.1175/2007MWR1858.1>.
- , and W.-C. Lee, 2012: Objective tropical cyclone center tracking using single-Doppler radar. *J. Appl. Meteor. Climatol.*, **51**, 878–896, <https://doi.org/10.1175/JAMC-D-11-0167.1>.
- Balachandran, S., D. R. Chavas, F. D. Marks Jr., S. Dubey, A. Shreevastava, and T. N. Krishnamurti, 2020: Characterizing the energetics of vortex-scale and sub-vortex-scale asymmetries during tropical cyclone rapid intensity changes. *J. Atmos. Sci.*, **77**, 315–336, <https://doi.org/10.1175/JAS-D-19-0067.1>.
- Bister, M., and K. A. Emanuel, 1997: The genesis of Hurricane Guillermo: TEXMEX analyses and a modeling study. *Mon. Wea. Rev.*, **125**, 2662–2682, [https://doi.org/10.1175/1520-0493\(1997\)125<2662:TGOHGT>2.0.CO;2](https://doi.org/10.1175/1520-0493(1997)125<2662:TGOHGT>2.0.CO;2).
- Bryan, G. H., and J. M. Fritsch, 2002: A benchmark simulation for moist nonhydrostatic numerical models. *Mon. Wea. Rev.*, **130**, 2917–2928, [https://doi.org/10.1175/1520-0493\(2002\)130<2917:ABSFMN>2.0.CO;2](https://doi.org/10.1175/1520-0493(2002)130<2917:ABSFMN>2.0.CO;2).
- , and H. Morrison, 2012: Sensitivity of a simulated squall line to horizontal resolution and parameterization of microphysics. *Mon. Wea. Rev.*, **140**, 202–225, <https://doi.org/10.1175/MWR-D-11-00046.1>.
- , R. P. Worsnop, J. K. Lundquist, and J. A. Zhang, 2017: A simple method for simulating wind profiles in the boundary layer of tropical cyclones. *Bound.-Layer Meteor.*, **162**, 475–502, <https://doi.org/10.1007/s10546-016-0207-0>.
- Cha, T.-Y., M. M. Bell, W.-C. Lee, and A. J. DesRosiers, 2021: Polygonal eyewall asymmetries during the rapid intensification of Hurricane Michael (2018). *Geophys. Res. Lett.*, **47**, e2020GL087919, <https://doi.org/10.1029/2020GL087919>.
- Dunion, J. P., 2011: Rewriting the climatology of the tropical North Atlantic and Caribbean Sea atmosphere. *J. Climate*, **24**, 893–908, <https://doi.org/10.1175/2010JCLI3496.1>.
- Gray, W. M., 1998: The formation of tropical cyclones. *Meteor. Atmos. Phys.*, **67**, 37–69, <https://doi.org/10.1007/BF01277501>.
- Guinn, T. A., and W. H. Schubert, 1993: Hurricane spiral bands. *J. Atmos. Sci.*, **50**, 3380–3403, [https://doi.org/10.1175/1520-0469\(1993\)050<3380:HSB>2.0.CO;2](https://doi.org/10.1175/1520-0469(1993)050<3380:HSB>2.0.CO;2).
- Hack, J. J., and W. H. Schubert, 1986: Nonlinear response of atmospheric vortices to heating by organized cumulus convection. *J. Atmos. Sci.*, **43**, 1559–1573, [https://doi.org/10.1175/1520-0469\(1986\)043<1559:NROAVT>2.0.CO;2](https://doi.org/10.1175/1520-0469(1986)043<1559:NROAVT>2.0.CO;2).
- Hankinson, M. C. N., M. J. Reeder, N. E. Davidson, and K. Puri, 2014: Vacillation cycles in simulations of Hurricane Katrina. *Quart. J. Roy. Meteor. Soc.*, **140**, 1878–1888, <https://doi.org/10.1002/qj.2275>.
- Hardy, S., J. Schwendike, R. K. Smith, C. J. Short, M. J. Reeder, and C. E. Birch, 2021: Fluctuations in inner-core structure during the rapid intensification of Super Typhoon Nepartak (2016). *Mon. Wea. Rev.*, **149**, 221–243, <https://doi.org/10.1175/MWR-D-19-0415.1>.
- Hausman, S. A., V. K. Ooyama, and W. H. Schubert, 2006: Potential vorticity structure of simulated hurricanes. *J. Atmos. Sci.*, **63**, 87–108, <https://doi.org/10.1175/JAS3601.1>.
- Haynes, P. H., and M. E. McIntyre, 1987: On the evolution of vorticity and potential vorticity in the presence of diabatic heating and frictional or other forces. *J. Atmos. Sci.*, **44**, 828–841, [https://doi.org/10.1175/1520-0469\(1987\)044<0828:OTEVOA>2.0.CO;2](https://doi.org/10.1175/1520-0469(1987)044<0828:OTEVOA>2.0.CO;2).
- Hendricks, E. A., and W. H. Schubert, 2010: Adiabatic rearrangement of hollow PV towers. *J. Adv. Model. Earth Syst.*, **2**, 19, <https://doi.org/10.3894/JAMES.2010.2.8>.
- , M. T. Montgomery, and C. A. Davis, 2004: The role of “vortical” hot towers in the formation of Tropical Cyclone Diana (1984). *J. Atmos. Sci.*, **61**, 1209–1232, [https://doi.org/10.1175/1520-0469\(2004\)061<1209:TROVHT>2.0.CO;2](https://doi.org/10.1175/1520-0469(2004)061<1209:TROVHT>2.0.CO;2).
- , W. H. Schubert, R. K. Taft, H. Wang, and J. P. Kossin, 2009: Life cycles of hurricane-like vorticity rings. *J. Atmos. Sci.*, **66**, 705–722, <https://doi.org/10.1175/2008JAS2820.1>.
- , B. D. McNoldy, and W. H. Schubert, 2012: Observed inner-core structural variability in Hurricane Dolly (2008). *Mon. Wea. Rev.*, **140**, 4066–4077, <https://doi.org/10.1175/MWR-D-12-00018.1>.
- , W. H. Schubert, Y.-H. Chen, H.-C. Kuo, and M. S. Peng, 2014: Hurricane eyewall evolution in a forced shallow-water model. *J. Atmos. Sci.*, **71**, 1623–1643, <https://doi.org/10.1175/JAS-D-13-0303.1>.
- Kaplan, J., M. DeMaria, and J. A. Knaff, 2010: A revised tropical cyclone rapid intensification index for the Atlantic and eastern North Pacific basins. *Wea. Forecasting*, **25**, 220–241, <https://doi.org/10.1175/2009WAF2222280.1>.
- Kossin, J. P., and M. D. Eastin, 2001: Two distinct regimes in the kinematic and thermodynamic structure of the hurricane eye and eyewall. *J. Atmos. Sci.*, **58**, 1079–1090, [https://doi.org/10.1175/1520-0469\(2001\)058<1079:TDRITK>2.0.CO;2](https://doi.org/10.1175/1520-0469(2001)058<1079:TDRITK>2.0.CO;2).
- , and W. H. Schubert, 2001: Mesovortices, polygonal flow patterns, and rapid pressure falls in hurricane-like vortices. *J. Atmos. Sci.*, **58**, 2196–2209, [https://doi.org/10.1175/1520-0469\(2001\)058<2196:MPFPAR>2.0.CO;2](https://doi.org/10.1175/1520-0469(2001)058<2196:MPFPAR>2.0.CO;2).
- , B. D. McNoldy, and W. H. Schubert, 2002: Vortical swirls in hurricane eye clouds. *Mon. Wea. Rev.*, **130**, 3144–3149, [https://doi.org/10.1175/1520-0493\(2002\)130<3144:VSIHEC>2.0.CO;2](https://doi.org/10.1175/1520-0493(2002)130<3144:VSIHEC>2.0.CO;2).

- Kuo, H.-C., R. T. Williams, and J.-H. Chen, 1999: A possible mechanism for the eye rotation of Typhoon Herb. *Bull. Amer. Meteor. Soc.*, **56**, 1659–1673, [https://doi.org/10.1175/1520-0469\(1999\)056<1659:APMFTE>2.0.CO;2](https://doi.org/10.1175/1520-0469(1999)056<1659:APMFTE>2.0.CO;2).
- Lewis, B. M., and H. F. Hawkins, 1982: Polygonal eye walls and rainbands in hurricanes. *Bull. Amer. Meteor. Soc.*, **63**, 1294–1300, [https://doi.org/10.1175/1520-0477\(1982\)063<1294:PEWARD>2.0.CO;2](https://doi.org/10.1175/1520-0477(1982)063<1294:PEWARD>2.0.CO;2).
- Martinez, J., 2020: Axisymmetric and asymmetric processes contributing to tropical cyclone intensification and expansion. Ph.D. thesis, Colorado State University, 166 pp.
- McBride, J. L., and R. Zehr, 1981: Observational analysis of tropical cyclone formation. Part II: Comparison of non-developing versus developing systems. *J. Atmos. Sci.*, **38**, 1132–1151, [https://doi.org/10.1175/1520-0469\(1981\)038<1132:OAOATCF>2.0.CO;2](https://doi.org/10.1175/1520-0469(1981)038<1132:OAOATCF>2.0.CO;2).
- Miyamoto, Y., and T. Takemi, 2013: A transition mechanism for the spontaneous axisymmetric intensification of tropical cyclones. *J. Atmos. Sci.*, **70**, 112–129, <https://doi.org/10.1175/JAS-D-11-0285.1>.
- , and D. S. Nolan, 2018: Structural changes preceding rapid intensification in tropical cyclones as shown in a large ensemble of idealized simulations. *J. Atmos. Sci.*, **75**, 555–569, <https://doi.org/10.1175/JAS-D-17-0177.1>.
- Möller, J. D., and M. T. Montgomery, 2000: Tropical cyclone evolution via potential vorticity anomalies in a three-dimensional balance model. *J. Atmos. Sci.*, **57**, 3366–3387, [https://doi.org/10.1175/1520-0469\(2000\)057<3366:TCEVPV>2.0.CO;2](https://doi.org/10.1175/1520-0469(2000)057<3366:TCEVPV>2.0.CO;2).
- Montgomery, M. T., and R. J. Kallenbach, 1997: A theory for vortex Rossby-waves and its application to spiral bands and intensity changes in hurricanes. *Quart. J. Roy. Meteor. Soc.*, **123**, 435–465, <https://doi.org/10.1002/qj.49712353810>.
- , and R. K. Smith, 2017: Recent developments in the fluid dynamics of tropical cyclones. *Annu. Rev. Fluid Mech.*, **49**, 541–574, <https://doi.org/10.1146/annurev-fluid-010816-060022>.
- , M. E. Nicholls, T. A. Cram, and A. B. Saunders, 2006: A vertical hot tower route to tropical cyclogenesis. *J. Atmos. Sci.*, **63**, 355–386, <https://doi.org/10.1175/JAS3604.1>.
- , and Coauthors, 2012: The Pre-Depression Investigation of Cloud Systems in the Tropics (PREDICT) experiment: Scientific basis, new analysis tools, and some first results. *Bull. Amer. Meteor. Soc.*, **93**, 153–172, <https://doi.org/10.1175/BAMS-D-11-00046.1>.
- , G. Kilroy, R. K. Smith, and N. Črnivec, 2021: Contribution of mean and eddy momentum processes to tropical cyclone intensification. *Quart. J. Roy. Meteor. Soc.*, **146**, 3101–3117, <https://doi.org/10.1002/qj.3837>.
- Muramatsu, T., 1986: The structure of polygonal eye of a typhoon. *J. Meteor. Soc. Japan*, **64**, 913–921, https://doi.org/10.2151/jmsj1965.64.6_913.
- Nguyen, M. C., M. J. Reeder, N. E. Davidson, R. K. Smith, and M. T. Montgomery, 2011: Inner-core oscillation cycles during the intensification of Hurricane Katrina. *Quart. J. Roy. Meteor. Soc.*, **137**, 829–844, <https://doi.org/10.1002/qj.823>.
- Nolan, D. S., 2007: What is the trigger for tropical cyclogenesis? *Aust. Meteor. Mag.*, **56**, 241–266.
- , and M. T. Montgomery, 2002: Nonhydrostatic, three-dimensional perturbations to balanced, hurricane-like vortices. Part I: Linearized formulation, stability, and evolution. *J. Atmos. Sci.*, **59**, 2989–3020, [https://doi.org/10.1175/1520-0469\(2002\)059<2989:NTDPTB>2.0.CO;2](https://doi.org/10.1175/1520-0469(2002)059<2989:NTDPTB>2.0.CO;2).
- , and L. D. Grasso, 2003: Nonhydrostatic, three-dimensional perturbations to balanced, hurricane-like vortices. Part II: Symmetric response and nonlinear simulations. *J. Atmos. Sci.*, **60**, 2717–2745, [https://doi.org/10.1175/1520-0469\(2003\)060<2717:NTPTBH>2.0.CO;2](https://doi.org/10.1175/1520-0469(2003)060<2717:NTPTBH>2.0.CO;2).
- , Y. Moon, and D. P. Stern, 2007: Tropical cyclone intensification from asymmetric convection: Energetics and efficiency. *J. Atmos. Sci.*, **64**, 3377–3405, <https://doi.org/10.1175/JAS3988.1>.
- , N. A. Dahl, G. H. Bryan, and R. Rotunno, 2017: Tornado vortex structure, intensity, and surface wind gusts in large-eddy simulations with fully developed turbulence. *J. Atmos. Sci.*, **74**, 1573–1597, <https://doi.org/10.1175/JAS-D-16-0258.1>.
- Pendergrass, A. G., and H. E. Willoughby, 2009: Diabatically induced secondary flows in tropical cyclones. Part I: Quasi-steady forcing. *Mon. Wea. Rev.*, **137**, 805–821, <https://doi.org/10.1175/2008MWR2657.1>.
- Persing, J., M. T. Montgomery, J. C. McWilliams, and R. K. Smith, 2013: Asymmetric and axisymmetric dynamics of tropical cyclones. *Atmos. Chem. Phys.*, **13**, 12299–12341, <https://doi.org/10.5194/acp-13-12299-2013>.
- Prasanth, S., D. R. Chavas, F. D. Marks Jr., S. Dubey, A. Shreevastava, and T. N. Krishnamurti, 2020: Characterizing the energetics of vortex-scale and sub-vortex-scale asymmetries during tropical cyclone rapid intensity changes. *J. Atmos. Sci.*, **77**, 315–336, <https://doi.org/10.1175/JAS-D-19-0067.1>.
- Raymond, D. J., and H. Jiang, 1990: A theory for long-lived mesoscale convective systems. *J. Atmos. Sci.*, **47**, 3067–3077, [https://doi.org/10.1175/1520-0469\(1990\)047<3067:ATFLMM>2.0.CO;2](https://doi.org/10.1175/1520-0469(1990)047<3067:ATFLMM>2.0.CO;2).
- , S. L. Sessions, and C. L. Carrillo, 2011: Thermodynamics of tropical cyclogenesis in the northwest Pacific. *J. Geophys. Res.*, **116**, D18101, <https://doi.org/10.1029/2011JD015624>.
- , S. Gjorgjevska, S. Sessions, and Z. Fuchs, 2014: Tropical cyclogenesis and mid-level vorticity. *Aust. Meteor. Oceanogr. J.*, **64**, 11–25, <https://doi.org/10.22499/2.6401.003>.
- Reasor, P. D., M. D. Eastin, and J. F. Gamache, 2009: Rapidly intensifying Hurricane Guillermo (1997). Part I: Low-wavenumber structure and evolution. *Mon. Wea. Rev.*, **137**, 603–631, <https://doi.org/10.1175/2008MWR2487.1>.
- Ritchie, E. A., and G. J. Holland, 1999: Large-scale patterns associated with tropical cyclogenesis in the western Pacific. *Mon. Wea. Rev.*, **127**, 2027–2043, [https://doi.org/10.1175/1520-0493\(1999\)127<2027:LSPAWT>2.0.CO;2](https://doi.org/10.1175/1520-0493(1999)127<2027:LSPAWT>2.0.CO;2).
- Rotunno, R., and K. A. Emanuel, 1987: An air-sea interaction theory for tropical cyclones. Part II: Evolutionary study using a nonhydrostatic axisymmetric numerical model. *J. Atmos. Sci.*, **44**, 542–561, [https://doi.org/10.1175/1520-0469\(1987\)044<0542:AAITFT>2.0.CO;2](https://doi.org/10.1175/1520-0469(1987)044<0542:AAITFT>2.0.CO;2).
- Rozoff, C. M., J. P. Kossin, W. H. Schubert, and P. J. Mulero, 2009: Internal control of hurricane intensity variability: The dual nature of potential vorticity mixing. *J. Atmos. Sci.*, **66**, 133–147, <https://doi.org/10.1175/2008JAS2717.1>.
- Ryglicki, R. D., and D. Hodges, 2016: A deeper analysis of center-finding techniques for tropical cyclones in mesoscale models. Part I: Low-wavenumber analysis. *J. Appl. Meteor. Climatol.*, **55**, 531–559, <https://doi.org/10.1175/JAMC-D-15-0125.1>.
- Schubert, W. H., and J. J. Hack, 1982: Inertial stability and tropical cyclone development. *J. Atmos. Sci.*, **39**, 1687–1697, [https://doi.org/10.1175/1520-0469\(1982\)039<1687:ISATCD>2.0.CO;2](https://doi.org/10.1175/1520-0469(1982)039<1687:ISATCD>2.0.CO;2).
- , and B. D. McNoldy, 2010: Application of the concepts of Rossby length and Rossby depth to tropical cyclone dynamics. *J. Adv. Model. Earth Syst.*, **2** (3), <https://doi.org/10.3894/JAMES.2010.2.7>.
- , M. T. Montgomery, R. K. Taft, T. A. Quinn, S. R. Fulton, J. Kossin, and J. P. Edwards, 1999: Polygonal eyewalls, asymmetric eye contraction, and potential vorticity mixing in

- hurricanes. *J. Atmos. Sci.*, **56**, 1197–1223, [https://doi.org/10.1175/1520-0469\(1999\)056<1197:PEAECA>2.0.CO;2](https://doi.org/10.1175/1520-0469(1999)056<1197:PEAECA>2.0.CO;2).
- Shapiro, L. J., and H. E. Willoughby, 1982: The response of balanced hurricanes to local sources of heat and momentum. *J. Atmos. Sci.*, **39**, 378–394, [https://doi.org/10.1175/1520-0469\(1982\)039<0378:TROBHT>2.0.CO;2](https://doi.org/10.1175/1520-0469(1982)039<0378:TROBHT>2.0.CO;2).
- Smith, R. K., G. Kilroy, and M. T. Montgomery, 2021: Tropical cyclone life cycle in a three-dimensional numerical simulation. *Quart. J. Roy. Meteor. Soc.*, **147**, 3373–3393, <https://doi.org/10.1002/qj.4133>.
- Tory, K. J., J. D. Kepert, J. A. Sippel, and C. M. Nguyen, 2012: On the use of potential vorticity tendency equations for diagnosing atmospheric dynamics in numerical models. *J. Atmos. Sci.*, **69**, 942–960, <https://doi.org/10.1175/JAS-D-10-05005.1>.
- Wissmeier, U., and R. K. Smith, 2011: Tropical cyclone convection: The effects of ambient vertical vorticity. *Quart. J. Roy. Meteor. Soc.*, **137**, 845–857, <https://doi.org/10.1002/qj.819>.
- Wurman, J., and K. Kosiba, 2018: The role of small-scale vortices in enhancing surface winds and damage in Hurricane Harvey (2017). *Mon. Wea. Rev.*, **146**, 713–722, <https://doi.org/10.1175/MWR-D-17-0327.1>.
- Yang, B., Y. Wang, and B. Wang, 2007: The effect of internally generated inner-core asymmetries on tropical cyclone potential intensity. *J. Atmos. Sci.*, **64**, 1165–1188, <https://doi.org/10.1175/JAS3971.1>.